

wFEM Heat Kernel: Discretization and Applications to Shape Analysis and Retrieval

Giuseppe Patané

Consiglio Nazionale delle Ricerche
Istituto di Matematica Applicata e Tecnologie Informatiche
patane@ge.imati.cnr.it

Abstract

Recent results in geometry processing have shown that shape segmentation, comparison, and analysis can be successfully addressed through the heat diffusion kernel. In this paper, we focus our attention on the properties (e.g., scale-invariance, semi-group property, robustness to noise) of the wFEM heat kernel, recently proposed in [PF10], and its application to shape comparison and feature-driven approximation. After proving that the wFEM heat kernel is intrinsically scale-covariant (i.e., without shape or kernel normalization) and scale-invariant through a normalization of the Laplacian eigenvalues, we experimentally verify that the wFEM heat kernel descriptors are more robust against shape/scale changes and provide better matching performances with respect to previous work. In the space $\mathcal{F}(\mathcal{M})$ of piecewise linear scalar functions defined on a triangle mesh \mathcal{M} , we introduce the wFEM heat kernel K_t , which is used to increase the degree of flexibility in the design of geometry-aware basis functions. Furthermore, we efficiently compute scale-based representations of maps on \mathcal{M} by specializing the Chebyshev method through the solution of a set of sparse linear systems, thus avoiding the spectral decomposition of the Laplacian matrix. Finally, the scalar product induced by K_t makes $\mathcal{F}(\mathcal{M})$ a Reproducing Kernel Hilbert Space, whose (reproducing) kernel is the linear FEM heat kernel, and induces the FEM diffusion distances on \mathcal{M} .

Keywords: Heat kernel, diffusion distances, shape comparison and retrieval, spectral analysis, finite element methods.

1. Introduction

Three main classes of maps are associated to the Laplace-Beltrami operator $\Delta: \mathcal{C}^2(\mathcal{N}) \rightarrow \mathcal{C}^0(\mathcal{N})$, where $\mathcal{C}^k(\mathcal{N})$ is the set of functions defined on a manifold \mathcal{N} and with order k of differentiability: the harmonic maps, the Laplacian eigenfunctions, and the solutions to the heat equation [Ros97]. Focusing on the last class, the *scale-based representation* $H: \mathcal{N} \times \mathbb{R} \rightarrow \mathbb{R}$ of the map $h: \mathcal{N} \subseteq \mathbb{R}^d \rightarrow \mathbb{R}$ is the solution to the *heat diffusion equation*

$$\begin{cases} \partial_t H(\mathbf{x}, t) = -\Delta H(\mathbf{x}, t) & (a) \\ H(\mathbf{x}, 0) = h(\mathbf{x}) & (b) \end{cases} \quad \mathbf{x} \in \mathcal{N}, \quad t \in \mathbb{R}, \quad (1)$$

and it can be written through the convolution operator \star as

$$\begin{cases} H(\mathbf{x}, t) := k_t(\mathbf{x}, \cdot) \star h = \int_{\mathcal{N}} k_t(\mathbf{x}, \mathbf{y}) h(\mathbf{y}) d\mathbf{y}, & (a) \\ k_t(\mathbf{x}, \mathbf{y}) := \sum_{i=1}^{+\infty} \exp(-\lambda_i t) \phi_i(\mathbf{x}) \phi_i(\mathbf{y}), & (b) \end{cases} \quad (2)$$

where k_t is the *heat diffusion kernel*. From the spectral decomposition (2b) of k_t , it follows that the Laplace-Beltrami and the heat diffusion operator have the same eigenfunctions $\{\phi_i\}_{i=1}^{+\infty}$. Disregarding a specific ordering of the Laplacian spectrum, each eigenvalue $\exp(-\lambda_i t)$ of the heat diffusion operator is associated to a corresponding Laplacian eigenvalue λ_i .

In geometry processing and shape analysis, several problems have been addressed through the properties of the heat diffusion kernel. Among them, we mention shape segmentation [dGGV08] and comparison [BK10; BGO11; DRW10;

GBAL09; OMMG10] through heat kernel shape descriptors, auto-diffusion maps [GBAL09; SOG09], and diffusion distances [BBK⁺10; CL06; LKC06]; dimensionality reduction [BN03; XHW10] with spectral embeddings; the computation of the gradient of discrete maps [Wan09] and the multi-scale approximation of functions [PF10]. In [VBCG10], prolongation operators have been used to extend the values of the heat diffusion kernel, computed on a low resolution representation of \mathcal{M} , to higher resolutions through the hierarchy associated to multiresolutive simplification algorithms.

Overview and contribution. In this context, we discuss the main properties of the wFEM heat kernel, recently presented in [PF10], and its applications to shape comparison and multi-scale approximation of scalar functions on surfaces. Assuming that the input manifold \mathcal{N} is approximated by a triangle mesh \mathcal{M} , let us introduce the space $\mathcal{F}(\mathcal{M})$ of piecewise linear maps defined on \mathcal{M} ; then, any function $f: \mathcal{M} \rightarrow \mathbb{R}$ in $\mathcal{F}(\mathcal{M})$ is uniquely identified by the array $\mathbf{f} := (f(\mathbf{p}_i))_{i=1}^n$ of its values at the mesh vertices $\{\mathbf{p}_i\}_{i=1}^n$. To guarantee the robustness of the wFEM heat kernel to surface discretization and its invariance to shape transformations, we replace the \mathcal{L}_2 scalar product in $\mathcal{F}(\mathcal{M})$ with the one $\langle \cdot, \cdot \rangle_B$ induced by the positive definite and symmetric mass matrix B associated to the linear FEM discretization $\tilde{L} := B^{-1}L$ of the Laplace-Beltrami operator [RWP06; VL08]. In this case, the *stiffness matrix* L is the un-normalized Tutte-Laplacian matrix with cotangent weights and the *mass matrix* B , or its lumped version, encodes the vari-

ation of the areas of the triangles or of the Voronoi regions of \mathcal{M} , respectively. In $\mathcal{F}(\mathcal{M})$, the *weighted scalar product* $\langle \mathbf{f}, \mathbf{g} \rangle_B := \mathbf{f}^T \mathbf{B} \mathbf{g}$, $\mathbf{f}, \mathbf{g} \in \mathcal{F}(\mathcal{M})$, generalizes the \mathcal{L}_2 product (i.e., $B := I$); is intrinsic to the surface on which the scalar functions are defined; and is adapted to the local sampling of \mathcal{M} through the variation of the triangle areas. Then, the *wFEM heat kernel* is discretized as $K_t := X D_t X^T B$, where $LX = BX\Delta$ is the generalized eigen-decomposition [GV89] of the couple (L, B) . Here, $X := [\mathbf{x}_1, \dots, \mathbf{x}_n]$ and $\Delta := \text{diag}(\lambda_i)_{i=1}^n$ are the matrices of the eigenvalues and eigenvectors of (L, B) , respectively. Through $\langle \cdot, \cdot \rangle_B$, we also introduce an *intrinsic* and *multi-scale* scalar product $\langle \cdot, \cdot \rangle_t$ in $\mathcal{F}(\mathcal{M})$ that makes K_t self-adjoint and $(\mathcal{F}(\mathcal{M}), \langle \cdot, \cdot \rangle_t)$ a *Reproducing Kernel Hilbert Space*. Then, we show that the Hilbert kernel of $\mathcal{F}(\mathcal{M})$ is the linear FEM heat kernel, whose entries uniquely define the diffusion distances on \mathcal{M} .

In $\mathcal{F}(\mathcal{M})$, the linear operator $K_t : \mathcal{F}(\mathcal{M}) \rightarrow \mathcal{F}(\mathcal{M})$, $\mathbf{f} \mapsto K_t \mathbf{f}$, induced by the wFEM heat kernel K_t , is *multi-scale* through the time parameter t ; *stable* under shape perturbations (e.g., sampling, connectivity, topological noise); and *invariant* to isometries. To efficiently compute the scale-based representation $K_t \mathbf{f}$, we specialize the Chebyshev method [CMV69; GV89; MVL03] to the wFEM heat kernel and evaluate $K_t \mathbf{f}$ through the solution of a set of sparse linear systems. In this case (Sect. 2.2) and assuming exact arithmetic, a rational Chebyshev function of degree (r, r) , with $r := 7$, provides an error lower than 10^{-7} , which is satisfactory for the approximation of $K_t \mathbf{f}$ on 3D shapes. If necessary, a higher approximation accuracy is achieved by slightly increasing the degree of the rational Chebyshev approximation. We also show that the Chebyshev method provides an accurate approximation of $K_t \mathbf{f}$, which is compared with the partial spectral representation used by previous work. Furthermore, the proposed computation does not require the spectral decomposition of the Laplacian matrix, multiresolutive prolongation operators, and user-defined parameters. Finally, we discuss the approximation accuracy and stability of the wFEM heat kernel to noise.

Exploiting the isomorphism between $\mathcal{F}(\mathcal{M})$ and \mathbb{R}^n , the canonical basis $\mathcal{E} := \{\mathbf{e}_i\}_{i=1}^n$ of \mathbb{R}^n can be interpreted as the set of trivial maps that take value one at a given vertex of \mathcal{M} and zero otherwise. Then, $\mathcal{B} := \{K_t \mathbf{e}_i\}_{i=1}^n$ can be considered as a smooth counterpart of \mathcal{E} in $\mathcal{F}(\mathcal{M})$, which is a multi-scale version of the geometry-aware functions [SCOIT05]. In this case, the definition and properties of \mathcal{B} are driven by the geometry of \mathcal{M} and not uniquely by its connectivity. According to the local point signatures [CJ97] and geodesic-based descriptors [HSKK01; GSCO07; OMMG10], each map $K_t \mathbf{e}_i$, which is analogous to the diffusion wavelets and maps [CL06], summarizes the shape distribution in a neighborhood of \mathbf{p}_i . This basis is also used to compute a topology-driven approximation of noisy maps and to distinguish their local and global component. To automatically select the elements of \mathcal{B} that better characterize $\mathcal{F}(\mathcal{M})$ and encode the geometric properties of \mathcal{M} , we consider the basis functions $\{K_t \mathbf{e}_i\}_i$ centered at the critical points of the Laplacian eigenfunctions [RPSS10] or of the auto-diffusion maps [GBAL09].

Comparison with previous work. According to the spectral representation of the heat kernel in Eq. (2b), the spectrum of the Laplacian matrix with FEM, Voronoi-cot, and cotangent weights is used to compute the discrete heat kernel as $\tilde{K}_t := X D_t X^T$ [BK10; dGGV08; GBAL09; Wan09]. Comparing the kernels \tilde{K}_t and K_t , we notice that $K_t = \tilde{K}_t B$ and that the wFEM discretization explicitly involves the mass matrix B . In this case, \tilde{K}_t is scale-dependent; i.e., rescaling \mathcal{M} to $\alpha \mathcal{M}$, $\alpha > 0$, \tilde{K}_t changes according to the relation $\tilde{K}_t(\alpha \mathcal{M}) = \alpha^{-2} \tilde{K}_{\alpha^{-2}t}(\mathcal{M})$. It follows that both the geometric and temporal component of $\tilde{K}_t(\alpha \mathcal{M})$ is affected by the surface rescaling and the corresponding heat kernel shape descriptors cannot be directly used for matching. To overcome this drawback, previous work reshapes the surface to have unit area before computing the heat kernel or normalizes the kernel itself. However, shape normalization is not sufficient when dealing with partially-sampled surfaces or when local re-scalings have been applied. Alternatively, the scale-invariance of \tilde{K}_t can be induced in the Fourier domain [BK10] with a normalization that is neither unique nor inherent to the input shape.

If the mass matrix B is lumped to the positive diagonal matrix D , then the wFEM heat kernel $K_t := X D_t X^T B$ becomes equal to the discretization $K_t^* := X D_t X^T D$, which holds for Laplacians of type $L := D^{-1}W$ [BBGO11; OMMG10; Rus07; SOG09; VBCG10]. Here, W has the mask of the mesh adjacency matrix and the diagonal entries of D are the areas of the Voronoi regions associated to the vertices of \mathcal{M} . Indeed, K_t can be considered as the generalization of K_t^* . Using the mass matrix B instead of its lumped version D allows us to accurately encode the geometry of the input surface through the area of its triangles instead of its Voronoi regions. In this way (Sect. 5), the wFEM heat kernel descriptors and the corresponding FEM distances have a higher robustness against topological and scale changes, irregular sampling, and noise. Furthermore, K_t is intrinsically scale-covariant (i.e., without shape or kernel normalization) and scale-invariant through a normalization of the Laplacian eigenvalues. To show these properties, we evaluate the matching performances of the wFEM heat kernel descriptors on the SHREC'10 data set [BBB⁺10; BBC⁺10] and compare our results with previous work.

The paper is organized as follows. The wFEM heat kernel, its computation, and the corresponding diffusion distances are presented in Sect. 2 and 3. The canonical basis, the feature-driven approximation, and applications to shape comparison are discussed in Sect. 4 and 5. Future work is outlined in Sect. 6.

2. wFEM heat kernel

We briefly recall the weak formulation of the heat equation, introduce its discretization with respect to linear finite elements [PF10] (Sect. 2.1), and discuss the computation of its solution through the Chebyshev method (Sect. 2.2). Finally, we present the main features of the proposed approach and discretization with respect to previous work (Sect. 2.3).

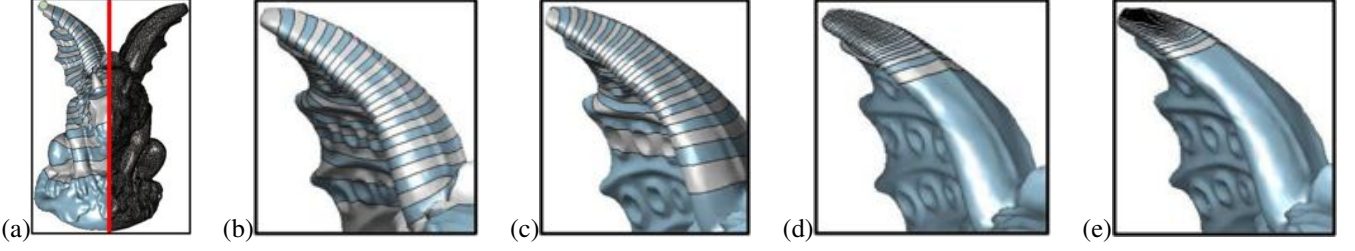


Figure 1: (a) Basis function $K_t \mathbf{e}_i$ centered at the green point, which is located in the upper part of the left wing, and computed with the generalized Chebyshev method and (b-e) different values of the time parameter t .

2.1. Weak formulation of the heat equation

Multiplying Eq. (1a) with a test function $\psi \in \mathcal{C}^2$, integrating the resulting relation over \mathcal{N} , and using the Green formula, we get the weak formulation

$$\langle \psi, \partial_t H \rangle_{\mathcal{L}_2(\mathcal{N})} + \langle \nabla H, \nabla \psi \rangle_{\mathcal{L}_2(\mathcal{N})} = 0,$$

where $\langle h_1, h_2 \rangle_{\mathcal{L}_2(\mathcal{N})} := \int_{\mathcal{N}} h_1(\mathbf{p}) h_2(\mathbf{p}) d\mathbf{p}$ is the $\mathcal{L}_2(\mathcal{N})$ scalar product. To apply the Green formula and ensure the differentiability of the solution to Eq. (1a), we assume that the test functions satisfy trivial value/boundary conditions. For 3D surfaces, the solution to the previous differential equation is approximated in the space $\mathcal{F}(\mathcal{M})$ of piecewise linear functions defined over a triangulation $\mathcal{M} := (M, T)$ of \mathcal{N} . Here, $M := \{\mathbf{p}_i\}_{i=1}^n$ is a set of n vertices and T is the mesh adjacency graph. Applying the Galerkin method with linear finite elements $\mathcal{S} := \{\psi_i\}_{i=1}^n$ on \mathcal{M} , the solution $H(\mathbf{x}, t)$ is approximated by $\tilde{H}(\mathbf{x}, t) := \sum_{i=1}^n \alpha_i(t) \psi_i(\mathbf{x})$, where the vector $\alpha(t) := (\alpha_i(t))_{i=1}^n$ satisfies the system $B \partial_t \alpha(t) + L \alpha(t) = \mathbf{0}$ of first order differential equations. Since B is positive definite, the previous equation becomes $[\partial_t + B^{-1}L] \alpha(t) = \mathbf{0}$. Then, the Laplace-Beltrami operator is approximated by the *weighted Laplacian matrix* $\tilde{L} := B^{-1}L$ and Eq. (1) is discretized as

$$\begin{cases} \partial_t F(\mathbf{p}, t) = -\tilde{L}F(\mathbf{p}, t), & \mathbf{p} \in \mathcal{M}, \\ F(\mathbf{p}_i, 0) = f(\mathbf{p}_i), & i = 1, \dots, n. \end{cases}$$

According to the linear FEM discretization of the Laplace-Beltrami operator [RWP06; VL08], the *stiffness matrix* L is the un-normalized Tutte-Laplacian matrix with cotangent weights and the *mass matrix* B encodes the geometry of \mathcal{M} in terms of triangle areas. More precisely, these matrices are defined as

$$B(i, j) := \begin{cases} \frac{|t_r| + |t_s|}{12} & j \in N(i), \\ \frac{\sum_{k \in N(i)} |t_k|}{6} & i = j, \\ 0 & \text{else,} \end{cases} \quad (3)$$

$$L(i, j) := \begin{cases} w(i, j) := \frac{\cot \alpha_{ij} + \cot \beta_{ij}}{2} & j \in N(i), \\ -\sum_{k \in N(i)} w(i, k) & i = j, \\ 0 & \text{else,} \end{cases}$$

where $N(i)$ is the 1-star of the vertex i ; α_{ij} , β_{ij} are the angles opposite to the edge (i, j) ; t_r , t_s are the triangles that share the edge (i, j) ; and $|t|$ is the area of the triangle t .

Recalling that the Laplacian eigenvectors $\{\mathbf{x}_i\}_{i=1}^n$, $L\mathbf{x}_i = \lambda_i B\mathbf{x}_i$, $\lambda_i \leq \lambda_{i+1}$, of the couple (L, B) in Eq. (3) are orthonormal with respect to the scalar product $\langle \cdot, \cdot \rangle_B$ induced by B , we have that

$$\langle \mathbf{x}_i, \mathbf{x}_j \rangle_B = \mathbf{x}_i^T B \mathbf{x}_j = \delta_{ij}, \quad i, j = 1, \dots, n \iff X^T B X = I, \quad (4)$$

with $X := [\mathbf{x}_1, \dots, \mathbf{x}_n]$ the matrix of the eigenvectors. Since the unknown function $F: \mathcal{M} \times \mathbb{R} \rightarrow \mathbb{R}$ is a $n \times 1$ vector for each value of the parameter t , the heat diffusion solution $F(\cdot, t)$ is expressed as a linear combination $F(\cdot, t) = \sum_{i=1}^n \alpha_i(t) \mathbf{x}_i$ of the eigensystem of (L, B) , where $\alpha(t) := (\alpha_i(t))_{i=1}^n$ is the unknown vector. Using the previous relation, the identity $\mathbf{f} = \sum_{i=1}^n \langle \mathbf{f}, \mathbf{x}_i \rangle_B \mathbf{x}_i$, the invertibility of the matrix B , and the linear independence of the Laplacian eigenfunctions, each component $\alpha_i(t)$ satisfies the differential equation $\alpha_i'(t) + \lambda_i \alpha_i(t) = 0$, with boundary condition $\alpha_i(0) = \langle \mathbf{f}, \mathbf{x}_i \rangle_B$, $i = 1, \dots, n$, $\mathbf{f} := (f(\mathbf{p}_i))_{i=1}^n$. Indeed, the *scale-based representation* of $f: \mathcal{M} \rightarrow \mathbb{R}$ is

$$F(\cdot, t) = \sum_{i=1}^n \exp(-\lambda_i t) \langle \mathbf{f}, \mathbf{x}_i \rangle_B \mathbf{x}_i, \quad t \in \mathbb{R}, \quad (5)$$

which is re-written in matrix form as $F(\cdot, t) = K_t \mathbf{f}$, where

$$K_t := X D_t X^T B, \quad D_t := \text{diag}(\exp(-\lambda_i t))_{i=1}^n, \quad (6)$$

is the *weighted linear FEM (wFEM) heat kernel matrix*. Lumping the mass matrix B , we get the diagonal matrix $D := \text{diag}(d(i))_{i=1}^n$, whose entries are the areas $d(i) := \frac{1}{3} \sum_{j \in N(i)} |t_j|$ of the Voronoi regions of \mathcal{M} , and K_t becomes equal to the *Voronoi-cot (or lumped FEM) heat kernel*

$$K_t^* := X D_t X^T D, \quad L X = X \Delta, \quad (7)$$

used by previous work [BBGO11; OMMG10; Rus07; SOG09; VBCG10]. It follows that the wFEM heat kernel generalizes K_t^* ; i.e., lumping the mass matrix B the corresponding wFEM heat kernel equals K_t^* . Choosing $B := I$ in Eq. (6), we get the *linear FEM heat kernel matrix* $\tilde{K}_t := X D_t X^T$. Table 1 summarizes the properties of different discretizations of the heat kernel.

2.2. Computation of the wFEM heat kernel

This section discusses three methods for the computation of the solution to the heat diffusion equation; i.e., (i) the spectral approach through the computation of the Laplacian spectrum of (L, B) ; (ii) the first order Taylor approximation, for

Table 1: Definition and properties of different discretizations of the heat kernel: sparsity, positive definiteness, and symmetry. The full \bullet and empty \circ circle means that the corresponding property is or is not satisfied, respectively.

Method	Matrix K_t	Sp.	Pos. Def.	Sym.
Std. HK	XD_tX^T	\circ	\bullet	\bullet
Vor.-cot HK	XD_tX^TD	\circ	\bullet	\circ
wFEM HK	XD_tX^TB	\circ	\bullet	\circ

small values of the time parameter; and (iii) the generalized Chebyshev method. Then, we show how the wFEM heat kernel has been used to define a geometric basis of $\mathcal{F}(\mathcal{M})$; address signal approximation; and define shape descriptors capable of distinguishing local/global features and discriminating similar shapes.

Spectral approach. The exponential decay of the filter factor $\sigma_i := \exp(-\lambda_i t)$ in (5) increases with λ_i and the computational bottleneck for evaluating the whole Laplacian spectrum imposes on us to consider only a part of the Laplacian spectrum. To this end, the sum in (5) is truncated by considering only the contribution related to the first k eigenpairs; i.e.,

$$F_k(\cdot, t) = \sum_{i=1}^k \exp(-\lambda_i t) \langle \mathbf{f}, \mathbf{x}_i \rangle_B \mathbf{x}_i = X_k D_t^{(k)} X_k^T \mathbf{B} \mathbf{f}, \quad t \in \mathbb{R}, \quad (8)$$

where $X_k := [\mathbf{x}_1, \dots, \mathbf{x}_k]$ is the $n \times k$ matrix of Laplacian eigenfunctions and $D_t^{(k)} := \text{diag}(\exp(-\lambda_i t))_{i=1}^k \in \text{GL}_k(\mathbb{R})$ is the diagonal matrix with the filter factors. If $t := 0$, then $F_k(\cdot, 0) = \sum_{i=1}^k \langle \mathbf{f}, \mathbf{x}_i \rangle_B \mathbf{x}_i$ is the least-squares approximation of f in the linear space generated by the first k eigenvectors and with respect to the norm $\|\cdot\|_B$. These eigenvalues and eigenvectors are computed in super-linear time [VL08].

First order Taylor approximation. Firstly, we verify that the derivative of K_t , at $t := 0$, equals $\tilde{L} := B^{-1}L$ and generalizes the first order Taylor approximation, which holds for $B := I$. From the identity

$$\begin{aligned} \frac{I - K_t}{t} &= \frac{1}{t} [I - XD_tX^TB] \\ &\stackrel{(4)}{=} \frac{1}{t} [X(I - D_t)X^{-1}] \\ &= X \text{diag} \left(\frac{1 - \exp(-\lambda_i t)}{t} \right)_{i=1}^n X^{-1}, \end{aligned}$$

and the relation $\lim_{t \rightarrow 0^+} t^{-1}(1 - \exp(-\lambda_i t)) = \lambda_i$, it follows that

$$\lim_{t \rightarrow 0^+} \frac{I - K_t}{t} = X \Delta X^{-1} = B^{-1}L.$$

Indeed, the wFEM heat kernel K_t is approximated by the matrix $(I - tB^{-1}L)$, $t \rightarrow 0^+$, and $K_t \mathbf{f}$ solves the sparse linear system

$$B(K_t \mathbf{f}) = (B - tL) \mathbf{f}, \quad t \rightarrow 0^+. \quad (9)$$

Then, Eq. (9) gives an approximation of $F(\cdot, t)$, $t \rightarrow 0^+$, that is independent of the Laplacian spectrum and is valid only for small values of t .

Generalized Chebyshev approximation. To evaluate $F(\cdot, t) := K_t \mathbf{f}$, for any $\mathbf{f} \in \mathbb{R}^n$, we specialize the Chebyshev method [CMV69; GV89; MVL03] to the wFEM heat kernel. To this end, we verify that the wFEM heat kernel matrix is still the exponential of the weighted Laplacian matrix; i.e., $K_t = \exp(-tB^{-1}L)$. We briefly recall that the rational Chebyshev approximation is based on the extension of the minmax Chebyshev theory to rational fractions; in this case, we compute the function $c_{rr}(x) := a_{rr}(x)/b_{rr}(x)$ that provides the best approximation of the exponential function with respect to the \mathcal{L}^∞ norm over the semi-axis $[0, +\infty)$; i.e.,

$$\|c_{rr}(x) - e^{-x}\|_{\mathcal{L}^\infty([0, +\infty))} = \min_{p_{rr} \in \mathcal{R}_{rr}} \{\|p_{rr}(x) - e^{-x}\|_\infty\}, \quad (10)$$

where \mathcal{R}_{rr} is the space of (r, r) -degree rational functions. Using algebraic rules, the solution to the problem (10) is rewritten as $c_{rr}(x) = \alpha_0 + \sum_{i=1}^r \alpha_i / (x - \theta_i)$ and the exponential matrix is approximated by

$$\exp(C) \approx \alpha_0 I + \sum_{i=1}^r \alpha_i (C - \theta_i I)^{-1}. \quad (11)$$

In this representation, the poles $\{\theta_i\}_{i=1}^r$ and the coefficients $\{\alpha_i\}_{i=1}^r$ have been computed for $r := 5, 7$ [GS92]. For a general degree r and a fixed value of t , the coefficients of the rational approximation of the exponential function are computed using the Padé method [GV89], which is implemented in standard numerical software packages.

To apply the Chebyshev method to the wFEM heat kernel, we firstly verify that K_t is the exponential of the weighted Laplacian matrix with respect to time; i.e., $K_t = \exp(-tB^{-1}L)$. From the matrix representation $B^{-1}L = X \Delta X^T B$ of the eigenvalue problem for (L, B) and the orthogonality relation (4), we get that $(B^{-1}L)^k = X \Delta^k X^T B$, $k \in \mathbb{N}$, and

$$\begin{aligned} \exp(-tB^{-1}L) &:= \sum_{k=0}^{+\infty} \frac{(-tB^{-1}L)^k}{k!} \\ &= \sum_{k=0}^{+\infty} \frac{(-t)^k}{k!} X \Delta^k X^T B \\ &= X \left[\sum_{k=0}^{+\infty} \frac{(-\Delta t)^k}{k!} \right] X^T B \\ &= X \text{diag} \left(\sum_{k=0}^{+\infty} \frac{(-\lambda_i t)^k}{k!} \right)_{i=1}^n X^T B \\ &= XD_tX^TB \\ &= K_t. \end{aligned}$$

Through the identity in Eq. (11), $\exp(C) \mathbf{f}$ is approximated as $\exp(C) \mathbf{f} \approx \alpha_0 \mathbf{f} + \sum_{i=1}^r \alpha_i (C - \theta_i I)^{-1} \mathbf{f}$; i.e., $\exp(C) \mathbf{f}$ is the sum of the solutions of r sparse linear systems

$$(C - \theta_i I) \mathbf{g}_i = \alpha_i \mathbf{f}, \quad i = 1, \dots, r. \quad (12)$$

Since we cannot explicitly invert the matrix B and apply the scheme to $C := -tB^{-1}L$, we notice that each vector in Eq.

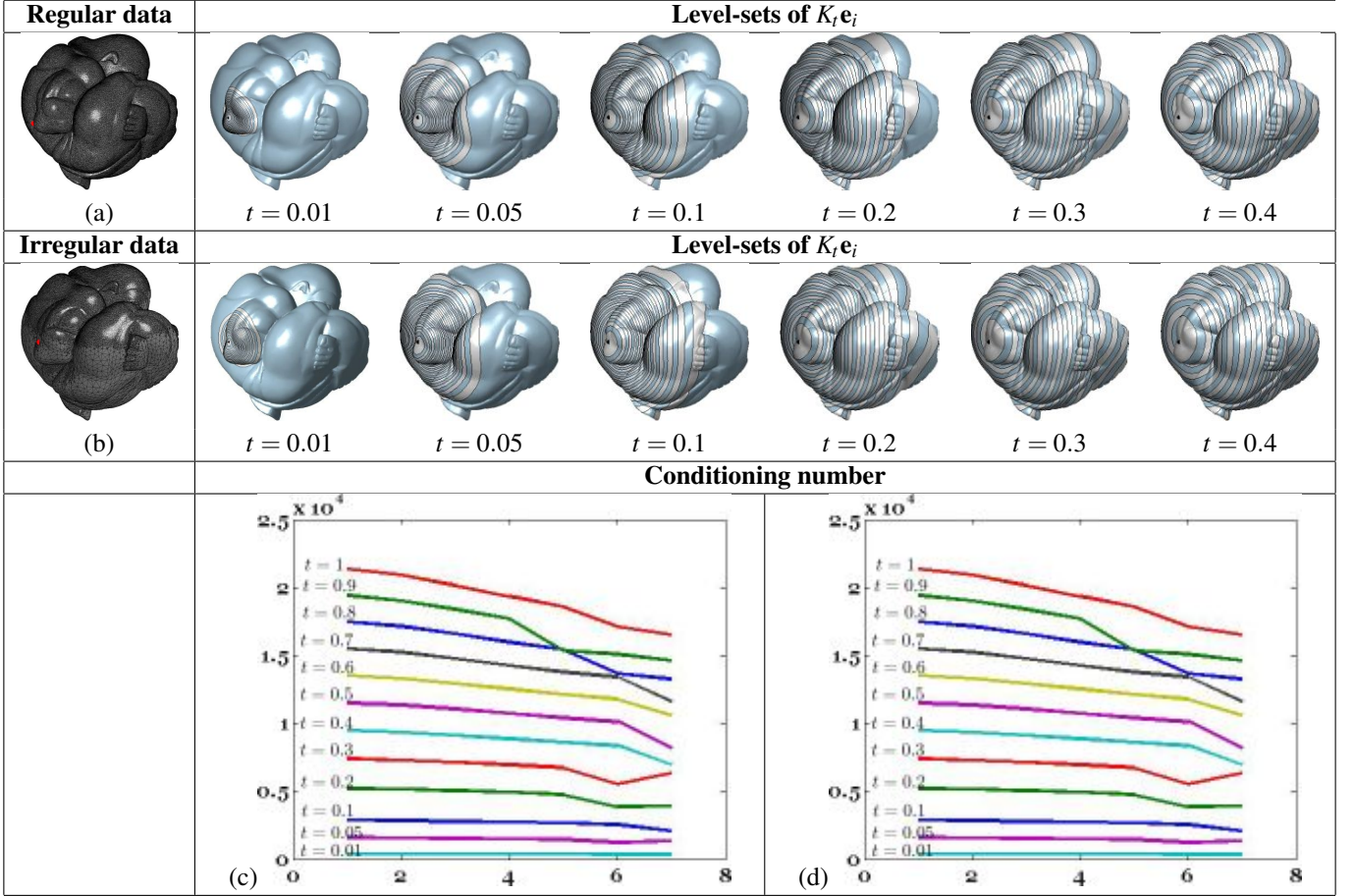


Figure 2: Level-sets of the function $K_t \mathbf{e}_i$, induced by the wFEM heat kernel and computed through the Chebyshev method, on (first row) the regularly- and (second row) the irregularly-sampled surfaces in (a,b). The anchor point \mathbf{p}_i (red dot) is placed on the elbow. (c,d) \mathcal{L}_2 conditioning numbers (y-axis) of the matrices $\{(tL + \theta_i B)\}_{i=1}^7$ in Eq. (13), for several values the time parameter t ; the indices of the coefficients $\{\theta_i\}_{i=1}^7$ are reported on the x-axis.

(12) solves the system $(tB^{-1}L + \theta_i I)\mathbf{g}_i = -\alpha_i \mathbf{f}$ if and only if $(tL + \theta_i B)\mathbf{g}_i = -\alpha_i B\mathbf{f}$. For any $i = 1, \dots, r$, \mathbf{g}_i is now calculated as the solution of a sparse linear system and $K_t \mathbf{f}$ is recovered as

$$K_t \mathbf{f} \approx \alpha_0 \mathbf{f} + \sum_{i=1}^r \mathbf{g}_i = \alpha_0 \mathbf{f} - \sum_{i=1}^r \alpha_i (tL + \theta_i B)^{-1} B\mathbf{f}. \quad (13)$$

The solution \mathbf{g}_i is computed by an iterative solver, which exploits the sparsity of the coefficient matrix $(tL + \theta_i B)$, without pre-factorizing the matrices L and B . Among the main solvers, we mention the Jacobi, Gauss-Seidel, and minimum residual methods (*minres*) [GV89]. Our implementation uses the *minres* procedure, which computes a minimum norm residual solution to the input linear system, whose coefficient matrix is symmetric, large, and sparse but not necessarily positive definite. Then, the overall cost of the computation of the value $K_t(i, i) = (K_t \mathbf{e}_i)^{(i)}$ at k feature points varies from $O(kn)$ to $O(kn^2)$, according to the sparsity of the coefficient matrix. Here, $\mathbf{v}^{(i)}$ is the i -th component of the vector \mathbf{v} . Selecting $B := I$ or $B := D$, the Chebyshev method also provides a new computation of the discrete heat diffusion kernel associated to the Laplacian matrix with cot and Voronoi-cot weights. We com-

pare these methods in Sect. 2.3.

Assuming exact arithmetic, the approximation error between $\exp(-tC)$ and its rational approximation $c_{rr}(tC)$ is estimated as

$$\|\exp(-tC) - c_{rr}(tC)\|_2 \leq \sigma_{rr}, \quad (14)$$

where σ_{rr} is the uniform rational Chebyshev constant [Var90]. Since this constant is known, independent of t , and related to the degree of the rational Chebyshev polynomial by the relation $\sigma_{rr} \approx 10^{-r}$, $r := 7$ provides an error lower than 10^{-7} , which is satisfactory for the approximation of $K_t \mathbf{f}$ on 3D shapes. If necessary, a higher approximation accuracy in Eq. (14) is achieved by slightly increasing the degree r . According to [MVL03], the Chebyshev approximation of the matrix $\exp(-tC)$ might be numerically unstable if $\|tC\|_2$ becomes large. From the upper bound $\|tB^{-1}L\|_2 \leq t\lambda_{\max}(L)\lambda_{\min}^{-1}(B)$, we get that a well-conditioned mass matrix B guarantees that $\|tB^{-1}L\|_2$ is bounded. These considerations and our experiments confirm that the Chebyshev method provides a good approximation accuracy and numerical stability for the computation of the discrete heat diffusion kernel. The Chebyshev method also avoids the evaluation of the Laplacian spectrum,

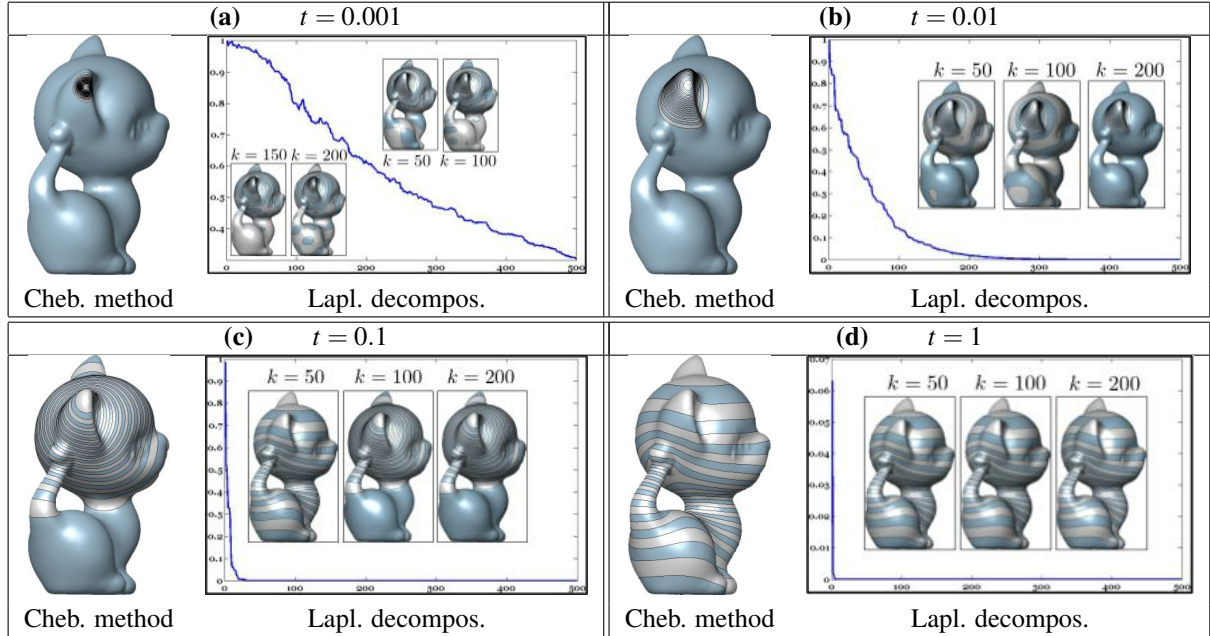


Figure 3: \mathcal{L}_∞ error (y-axis) between the Chebyshev approximation and the spectral representation (8) of the function $K_t \mathbf{e}_i$, computed using a different number k (x-axis) of eigenfunctions and values of the time parameter t .

which is unpractical in terms of computational and storage costs. These limitations are generally bypassed by approximating K_t with the eigenvectors related to the eigenvalues of smaller magnitude (c.f., Eq. (8)). While the Chebyshev computation is free of user-defined parameters, in [VBCG10] the resolution of the simplified approximation of the input surface, on which the Laplacian matrix is computed, and the number of Laplacian eigenpairs are tuned according to the value of the temporal variable.

2.3. Examples and discussions

Indicating with \mathbf{e}_i the i -th vector of the canonical basis of \mathbb{R}^n , $K_t \mathbf{e}_i$ is the map achieved by applying the diffusion process to the function that takes value one at the anchor \mathbf{p}_i and zero otherwise. For a detailed discussion on the properties of the functions $\{K_t \mathbf{e}_i\}_{i=1}^n$ and their application to feature-driven approximation of scalar functions, we refer the Reader to Sect. 4. Figs. 1, 2 show the level-sets of the map $K_t \mathbf{e}_i$ induced by the wFEM heat kernel and associated to several values of the time parameter. In Fig. 2, the analogous behavior of the level-sets confirms that the wFEM heat kernel is not affected by a different sampling (a,b) of the input surface. In both examples, $K_t \mathbf{e}_i$ has been computed using the Chebyshev method. According to Eq. (13), the value of t influences the conditioning number of the coefficient matrices $(tL + \theta_i B)$, $i = 1, \dots, r$. Our experiments (Fig. 2(c,d)) have shown that the linear systems in Eq. (12) are generally well-conditioned; in any case, pre-conditioners and regularization techniques [GV89] can be applied to attenuate numerical instabilities.

Fig. 3 shows the \mathcal{L}_∞ approximation error (y-axis) between the spectral representation (8) of $K_t \mathbf{e}_i$, computed using a differ-

ent number k (x-axis) of eigenfunctions, and the corresponding Chebyshev approximation (13). For small values of t (Fig. 3(a-b)), the spectral representation (8) requires a large number of Laplacian eigenvectors to recover local details. For large values of t (Fig. 3(c-d)), increasing k reduces the approximation error until it becomes almost constant and close to zero. In fact, in this case the behavior of $K_t \mathbf{e}_i$ is mainly influenced by the Laplacian eigenvectors related to the smaller eigenvalues. We conclude that the spectral representation generally requires a high number of eigenpairs without achieving an accuracy of the same order of the Chebyshev approximation, which involves only the solution of $r := 7$ sparse linear systems.

Figs. 4 and 5 show the stability of the wFEM heat diffusion with respect to the surface sampling density and noise, respectively. In Fig. 4, a higher resolution of \mathcal{M} improves the quality of the level-sets of the canonical basis function, which are always uniformly distributed around the anchor (black dot). In Fig. 5, an increase of the noise magnitude does not affect the shape and distribution of the level sets. Fig. 6 shows a canonical basis function $K_t \mathbf{e}_i$ associated to the wFEM and the Voronoi-cot heat kernel, computed using the corresponding partial spectral decomposition; e.g., (8) for the wFEM heat kernel. Fig. 7 shows the same basis function for the heat kernels associated to different weights of the Laplacian matrix and evaluated through the Chebyshev approximation; e.g., Eq. (13) for the wFEM heat kernel. Firstly, we notice the analogous behavior of the map $K_t \mathbf{e}_i$ computed using the wFEM heat kernel through the Chebyshev approximation (Fig. 7(c,f)) and the generalized eigendecomposition of (L, B) (Fig. 6(a-c,g-i)) on the regularly- and irregularly-sampled surfaces \mathcal{M} in Fig. 2(a,b). Comparing these results with Figs. 6(d-f) and Figs. 7(a,b), on regularly sampled data the cot, Voronoi-cot, and wFEM heat kernels pro-

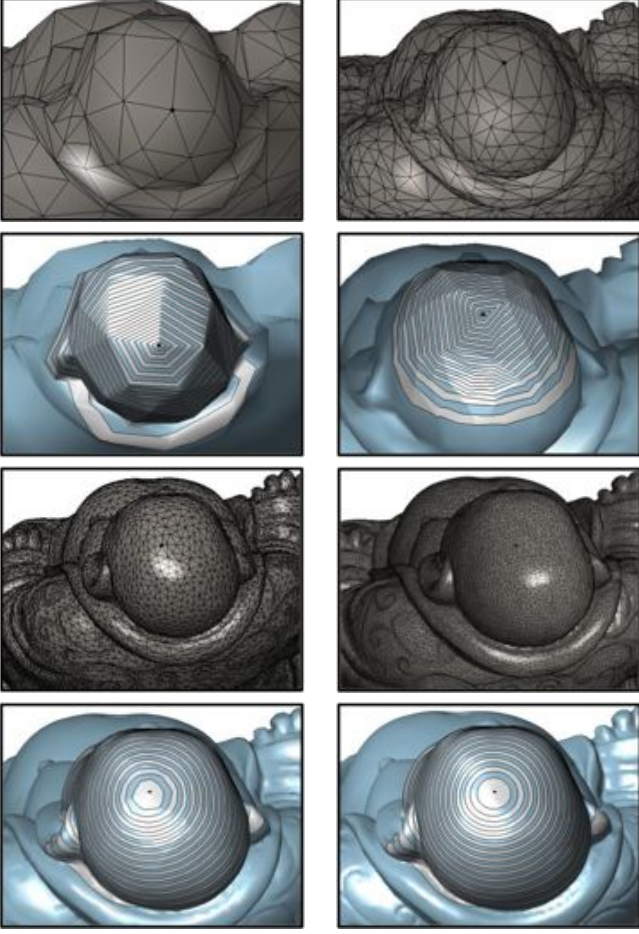


Figure 4: Smoothness of $K_t \mathbf{e}_i$ with respect to the sampling density of the input surface.

vide analogous results in terms of the level-sets of $K_t \mathbf{e}_i$. These results are also analogous to those achieved using the wFEM heat kernel on irregularly-sampled data (Figs. 6(g-i), 7(f)). Due to the uneven sampling of \mathcal{M} and the wide variation of the areas of its triangles, the quality of the approximation provided by the cot (Fig. 7(d)) and Voronoi-cot weights (Figs. 6(j-l), 7(e)) is lower.

We now compare the basis function $K_t^D \mathbf{e}_i := XD_t X^T D \mathbf{e}_i$ and $K_t \mathbf{e}_i := XD_t X^T B \mathbf{e}_i$, which are induced by the lumped FEM and wFEM heat kernel, respectively. As shown in Fig. 8, irregularly-sampled patches on \mathcal{M} generally affect the smoothness of $K_t^D \mathbf{e}_i$ at smaller scales; increasing t improves the smoothness of $K_t^D \mathbf{e}_i$ in terms of regularity of the level-sets and of a lower number of critical points. Comparisons with respect to the Taylor approximation (9) are shown in Fig. 9 and timings are reported in Table 2. Finally, the analogous behavior of the level-sets of $K_t \mathbf{e}_i$ (Fig. 10) and almost overlapped graphs of its values (Fig. 11) confirm the robustness of the wFEM heat kernel with respect to different shape transformations.

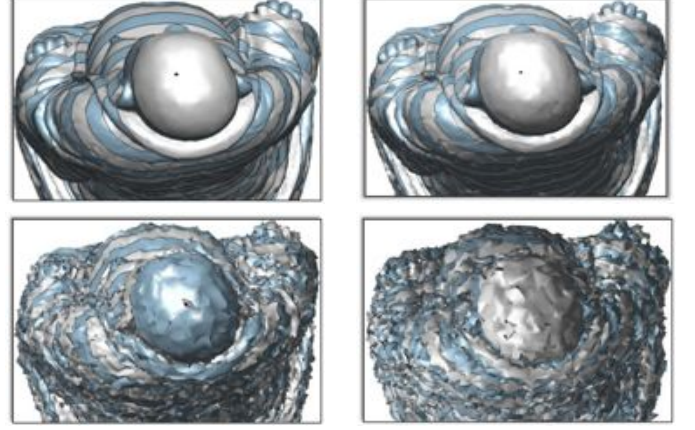


Figure 5: Smoothness of $K_t \mathbf{e}_i$ with respect to surfaces with an increasing noise magnitude.

3. wFEM heat kernel: properties and diffusion distances

As detailed in Proposition 3.1, in $\mathcal{F}(\mathcal{M})$ we introduce a time-dependent scalar product $\langle \cdot, \cdot \rangle_t$ that makes K_t self-adjoint and we verify that $(\mathcal{F}(\mathcal{M}), \langle \cdot, \cdot \rangle_t)$ is a Reproducing Kernel Hilbert Space. Furthermore, its reproducing kernel $H_t : \mathcal{M} \times \mathcal{M} \rightarrow \mathbb{R}$, which satisfies the reproduction property

$$\langle H_t(\cdot, \mathbf{p}_i), \mathbf{f} \rangle_t = f(\mathbf{p}_i), \quad i = 1, \dots, n, \quad (15)$$

is $H_t := \tilde{K}_{-t}$, where \tilde{K}_t is the linear FEM heat kernel (Sect. 2.1). In this way, computing the scalar product between $H_t(\cdot, \mathbf{p}_i)$ and f is equivalent to evaluate f at \mathbf{p}_i .

For the wFEM heat kernel, the diffusion distances cannot be defined by decomposing K_t as $Y^T Y$ or $Y^T B Y$; in fact, K_t is no longer symmetric. However, the self-adjointness of K_t with respect to the scalar product $\langle \cdot, \cdot \rangle_B$ allows us to introduce a time-dependent scalar product $\langle \cdot, \cdot \rangle_t$, which is induced by a symmetric and positive definite matrix S_t . Rewriting the entries of this matrix as $S_t(i, j) := \langle \mathbf{h}_i^t, \mathbf{h}_j^t \rangle_B$, or the entries of the Reproducing kernel as $H_t(i, j) := \langle \mathbf{g}_i^t, \mathbf{g}_j^t \rangle_B$, we extract the linear and wFEM diffusion distances on \mathcal{M} and show that the corresponding embeddings $\mathbf{g}_i^t := H_{t/2} \mathbf{e}_i$, $\mathbf{h}_i^t := K_{t/2} \mathbf{e}_i$ of each vertex \mathbf{p}_i of \mathcal{M} are evaluated through the Chebyshev approximation and without computing the generalized Laplacian spectrum.

Proposition 3.1. *Given a triangle mesh \mathcal{M} , let $LX = BX\Delta$ be the matrix representation of the linear FEM eigenvalue problem on \mathcal{M} . Here, $X := [\mathbf{x}_1, \dots, \mathbf{x}_n]$ and $\Delta := \text{diag}(\lambda_i)_{i=1}^n$ are the matrices of the generalized eigenvectors and eigenvalues of the couple (L, B) , respectively. Then, the following relations hold:*

- (A) *the wFEM heat kernel $K_t := XD_t X^T B$ is self-adjoint with respect to the scalar product induced by the mass matrix B . Furthermore, for any $\mathbf{f}, \mathbf{g} \in \mathcal{F}(\mathcal{M})$,*

$$\langle \mathbf{f}, \mathbf{g} \rangle_t := \langle K_t \mathbf{f}, \mathbf{g} \rangle_B = \langle \mathbf{f}, K_t \mathbf{g} \rangle_B = \mathbf{f}^T B X D_t X^T B \mathbf{g}, \quad (16)$$

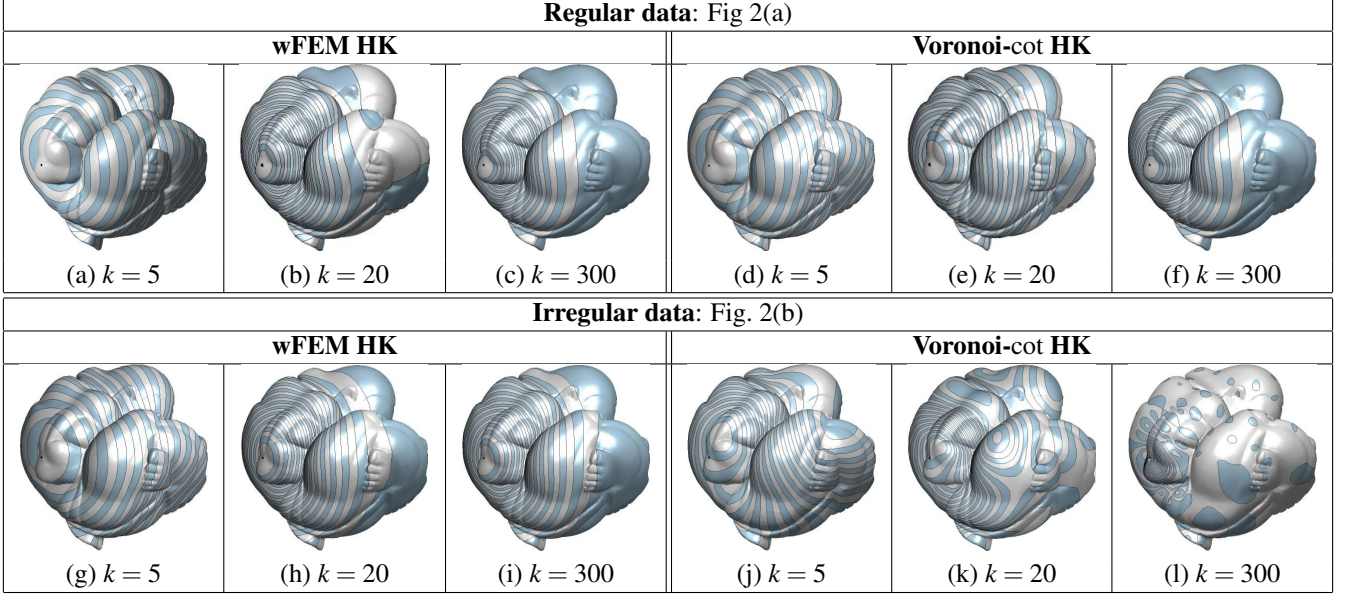


Figure 6: Approximation of the basis function $K_t \mathbf{e}_i$, $t = 0.1$, whose anchor is placed on the elbow (red point) of the regular and irregular surfaces in Fig. 2(a,b), with respect to the (a-c,g-i) wFEM and (d-f,j-l) Voronoi-cot weights, with a different number k of eigenfunctions. The Chebyshev approximation is shown in Fig. 7.

is a scalar product in $\mathcal{F}(\mathcal{M})$. In particular, the linear FEM Laplacian eigenfunctions $\{\mathbf{x}_i\}_{i=1}^n$ satisfy the relation

$$\|\mathbf{x}_i - \mathbf{x}_j\|_t^2 = \exp(\lambda_i t) + \exp(\lambda_j t), \quad i \neq j; \quad (17)$$

(B) $(\mathcal{F}(\mathcal{M}), \langle \cdot, \cdot \rangle_t)$ is a Reproducing Kernel Hilbert Space. The Hilbert kernel $H_t : \mathcal{M} \times \mathcal{M} \rightarrow \mathbb{R}$ that verifies the reproduction property (15) is the linear FEM heat kernel $H_t = \tilde{K}_{-t} = XD_{-t}X^T$;

(C) indicating with $S_t := BXD_tX^TB$ the matrix that induces the scalar product (16), we have that

$$\begin{cases} H_t(i, j) = \langle \mathbf{g}_i^t, \mathbf{g}_j^t \rangle_B, & \mathbf{g}_i^t = H_{t/2} \mathbf{e}_i & (a) \\ S_t(i, j) = \langle \mathbf{h}_i^t, \mathbf{h}_j^t \rangle_B, & \mathbf{h}_i^t = K_{t/2} \mathbf{e}_i & (b) \end{cases} \quad (18)$$

where the values of the linear and wFEM diffusion maps $\mathbf{g}_i^t, \mathbf{h}_i^t : \mathcal{M} \rightarrow \mathbb{R}$ are induced by the linear $\tilde{K}_{-t/2} = H_{t/2}$ and wFEM heat kernel K_t , respectively.

Proof. (A) To prove that K_t is self-adjoint with respect to $\langle \cdot, \cdot \rangle_B$ (i.e., $\langle K_t \mathbf{f}, \mathbf{g} \rangle_B = \langle \mathbf{f}, K_t \mathbf{g} \rangle_B$, $\mathbf{f}, \mathbf{g} \in \mathbb{R}^n$), we notice that

$$\begin{aligned} \langle \mathbf{f}, \mathbf{g} \rangle_t &= \langle K_t \mathbf{f}, \mathbf{g} \rangle_B \\ &= \mathbf{f}^T BXD_tX^TB \mathbf{g} \\ &= \mathbf{f}^T BK_t \mathbf{g} \\ &= \langle \mathbf{f}, K_t \mathbf{g} \rangle_B, \quad \mathbf{f}, \mathbf{g} \in \mathbb{R}^n. \end{aligned}$$

To prove that the scalar product in (16) is well-posed, we show that the matrix $S_t := BXD_tX^TB$ is symmetric and positive definite. From the identity $S_t =_{(4)} X^{-T} D_t X^{-1}$, we get that S_t is symmetric with strictly positive eigenvalues $(\exp(-\lambda_i t))_{i=1}^n$; indeed, S_t is also positive definite. To verify Eq. (17), we notice

that

$$\begin{aligned} \langle \mathbf{x}_i, \mathbf{x}_j \rangle_t &= \langle K_t \mathbf{x}_i, \mathbf{x}_j \rangle_B \\ &= \langle \exp(-\lambda_i t) \mathbf{x}_i, \mathbf{x}_j \rangle_B \\ &= \exp(-\lambda_i t) \delta_{ij}. \end{aligned}$$

(B) The reproduction property (15) is verified as follows

$$\begin{aligned} \langle H_t(\cdot, \mathbf{p}_i), f \rangle_t &= \langle H_t \mathbf{e}_i, \mathbf{f} \rangle_t \\ &=_{(16)} \mathbf{e}_i^T H_t BXD_tX^TB \mathbf{f} \\ &= \mathbf{e}_i^T XD_{-t}X^TBX D_tX^TB \mathbf{f} \\ &=_{(4)} \mathbf{e}_i^T XX^TB \mathbf{f} \\ &=_{(4)} \mathbf{e}_i^T \mathbf{f} \\ &= f(\mathbf{p}_i). \end{aligned}$$

We now show the uniqueness of the reproducing Hilbert kernel. Assuming that the matrices A_t and B_t satisfy the reproduction property and applying this property to the functions associated to each vector of the canonical basis $\{\mathbf{e}_i\}_{i=1}^n$ of \mathbb{R}^n , we get that

$$\mathbf{e}_i^T (A_t - B_t)^T BK_t \mathbf{e}_j = 0, \quad i, j = 1, \dots, n \quad \longleftrightarrow \quad A_t = B_t.$$

From the representation $H_t = XD_{-t}X^T = \tilde{K}_{-t}$, it follows that H_t is symmetric and positive definite.

(C) For the identity (18a), we notice that

$$\begin{aligned} H_{t/2} B H_{t/2} &= (XD_{-t/2}X^T) B (XD_{-t/2}X^T) \\ &=_{(4)} XD_{-t}X^T \\ &= H_t \end{aligned} \quad (19)$$

and therefore

$$H_t(i, j) = \mathbf{e}_i^T H_t \mathbf{e}_j =_{(19)} \langle H_{t/2} \mathbf{e}_i, H_{t/2} \mathbf{e}_j \rangle_B.$$

For the relation in Eq. (18b), we proceed in a similar way. From the identity

$$\begin{aligned} S_t &= BXD_{t/2}D_{t/2}X^TB \\ &\stackrel{(4)}{=} BXD_{t/2}(X^TBX)D_{t/2}X^TB \\ &= (BXD_{t/2}X^T)B(XD_{t/2}X^TB) \\ &= Y^TBY, \quad Y := XD_{t/2}X^TB = K_{t/2}, \end{aligned}$$

we get that

$$S_t(i, j) = \mathbf{e}_i^T S_t \mathbf{e}_j = \langle \mathbf{h}_i^t, \mathbf{h}_j^t \rangle_B, \quad \mathbf{h}_i^t := K_{t/2} \mathbf{e}_i.$$

□

To evaluate $\langle \mathbf{f}, \mathbf{g} \rangle_t = \mathbf{f}^T B(K_t \mathbf{g})$ in Eq. (16), we compute $K_t \mathbf{g}$ through the Chebyshev approximation; then, the resulting vector is multiplied by $\mathbf{f}^T B$. Let us now focus on the computation of the embedding of each vertex \mathbf{p}_i of \mathcal{M} as $\mathbf{g}_i^t := H_{t/2} \mathbf{e}_i$, in Eq. (18a). From the identity

$$H_t \mathbf{e}_i = XD_{-t} X^T B B^{-1} \mathbf{e}_i \iff \begin{cases} B \mathbf{y} = \mathbf{e}_i & (a) \\ H_t \mathbf{e}_i = XD_{-t} X^T B \mathbf{y} = K_{-t} \mathbf{y} & (b) \end{cases} \quad (20)$$

we get that $H_t \mathbf{e}_i$ is computed by applying the Chebyshev approximation (c.f., Eq. (20b)) to the vector \mathbf{y} that solves the sparse linear system in Eq. (20a). We also notice that the computation of K_{-t} is stable; in fact, it is achieved through the Chebyshev method and in a way analogous to the evaluation of K_t . The embedding of each vertex \mathbf{p}_i of \mathcal{M} associated to the Reproducing Kernel H_t is the canonical basis function $\mathbf{h}_i^t := K_{t/2} \mathbf{e}_i$, whose properties are discussed in Sect. 4.1. Finally, the corresponding linear and wFEM diffusion distances

$$\begin{cases} \|\mathbf{g}_i^t - \mathbf{g}_j^t\|_B^2 = H_{t/2}(i, i) - 2H_{t/2}(i, j) + H_{t/2}(j, j), \\ \|\mathbf{h}_i^t - \mathbf{h}_j^t\|_B^2 = K_{t/2}(i, i) - 2K_{t/2}(i, j) + K_{t/2}(j, j), \end{cases}$$

are uniquely defined by the entries of the matrices H_t and K_t , respectively. Indeed, the evaluation of the scalar product (16), the diffusion distances, and the embeddings are performed through the Chebyshev approximation and without computing of the Laplacian spectrum. The properties discussed in Proposition 3.1 apply to the wFEM heat kernel and are analogous to those that hold in the continuous case. This analogy confirms that the proposed discretization and the choice of the intrinsic scalar product $\langle \cdot, \cdot \rangle_B$ in $\mathcal{F}(\mathcal{M})$ maintain the main features of the heat diffusion kernel, together with a higher robustness to data discretization as compared to previous work.

4. Canonical basis and feature-driven approximation

In the space $\mathcal{F}(\mathcal{M})$ of piecewise linear maps defined on \mathcal{M} , the wFEM heat kernel is associated to the linear operator

$$\begin{aligned} K_t : \mathcal{F}(\mathcal{M}) &\rightarrow \mathcal{F}(\mathcal{M}) \\ \mathbf{f} &\mapsto K_t \mathbf{f} = XD_t X^T B \mathbf{f}. \end{aligned} \quad (21)$$

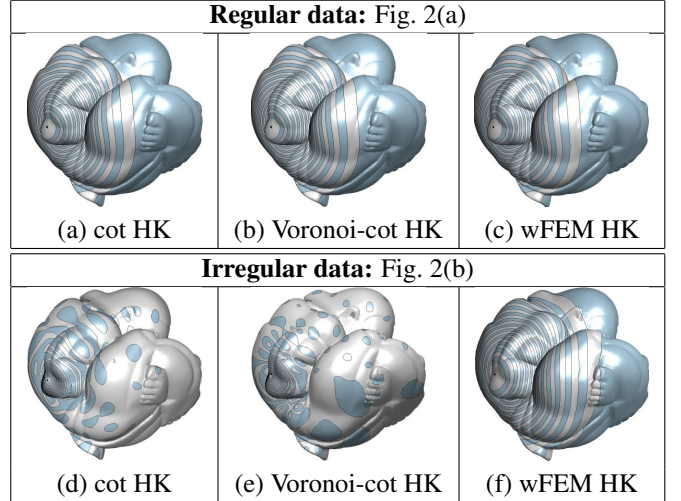


Figure 7: Chebyshev approximation of $K_t \mathbf{e}_i$, $t = 0.1$, with different weights of the Laplacian matrix.

In the following, K_t indicates both the wFEM heat kernel matrix and the induced linear operator (21). To introduce the canonical basis of $\mathcal{F}(\mathcal{M})$ (Sect. 4.1) and the feature-driven approximation (Sect. 4.2), we first show that the composition and the inverse of wFEM heat kernels is easily computed through the relations $K_{t_1} \circ K_{t_2} = K_{t_1+t_2}$ (*semi-group property*) and $K_t^{-1} = K_{-t}$ (*inversion property*). In fact,

$$\begin{aligned} K_{t_1+t_2} \mathbf{f} &= XD_{t_1+t_2} X^T B \mathbf{f} \\ &= XD_{t_1} D_{t_2} X^T B \mathbf{f} \\ &\stackrel{(4)}{=} XD_{t_1} (X^T B X) D_{t_2} X^T B \mathbf{f} \\ &= K_{t_1} K_{t_2} \mathbf{f}. \end{aligned}$$

In particular, the wFEM heat kernel satisfies the *commutative property*; i.e., $K_{t_1} \circ K_{t_2} = K_{t_2} \circ K_{t_1}$. For the inversion property, we notice that $K_t = XD_t X^T B = XD_t X^{-1}$ and therefore

$$K_t^{-1} \mathbf{f} = XD_{-t} X^{-1} \mathbf{f} = K_{-t} \mathbf{f}.$$

The wFEM heat kernel satisfies the heat equation $\partial_t(K_t \mathbf{f}) = -B^{-1} L K_t \mathbf{f}$ as well; in fact,

$$\begin{aligned} \partial_t K_t \mathbf{f} &= - \sum_{i=1}^n \lambda_i \exp(-\lambda_i t) \langle \mathbf{f}, \mathbf{x}_i \rangle_B \mathbf{x}_i, \\ L K_t \mathbf{f} &= \sum_{i=1}^n \exp(-\lambda_i t) \langle \mathbf{f}, \mathbf{x}_i \rangle_B L \mathbf{x}_i \\ &= \sum_{i=1}^n \exp(-\lambda_i t) \langle \mathbf{f}, \mathbf{x}_i \rangle_B (\lambda_i B \mathbf{x}_i) \\ &= -B \partial_t K_t \mathbf{f}. \end{aligned}$$

4.1. Canonical basis in $\mathcal{F}(\mathcal{M})$

Even though the Laplacian eigenvectors are intrinsic to the input surface, they can be computed only for a small set of eigenvalues and do not provide a flexible alignment of the function

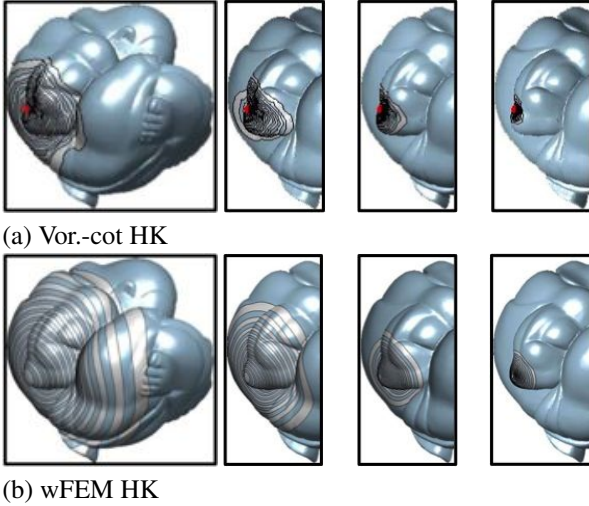


Figure 8: Level-sets of the basis $K_t \mathbf{e}_i$ induced by the (a) Voronoi-cot and (b) wFEM heat kernel on the irregularly-sampled surface in Fig. 2(b) with respect to different values of the time parameter. In (a,b), we have used the Chebyshev method and the same values of the time parameter.

behavior to specific shape features. Furthermore, the global support of the Laplacian eigenfunctions is a possible limitation to applications such as shape modification and compression, which benefit for a compact support in order to guarantee the locality of the deformation and improve the quantization effects. The geometry-aware maps [SC0IT05] provide a computationally efficient way to encode the local geometric information of \mathcal{M} ; however, they are designed for compression and based only on the connectivity of the input mesh.

Since K_t is invertible, the basis $\mathcal{E} := \{\mathbf{e}_i\}_{i=1}^n$ is mapped to a new canonical basis $\mathcal{B} := \{K_t \mathbf{e}_i\}_{i=1}^n$ of $\mathcal{F}(\mathcal{M})$, whose elements have a smooth behavior on \mathcal{M} and are intrinsically defined by \mathcal{M} . Starting from $t := 0$ and increasing t , the map $K_t \mathbf{e}_i$ changes from the Dirichlet function to a constant map. In fact, recalling that the eigenvalue $\lambda_1 = 0$ is associated to the eigenvector $\mathbf{1}$ and using the relation

$$K_t \mathbf{e}_i = \langle \mathbf{1}, \mathbf{e}_i \rangle_B \mathbf{1} + \sum_{i=2}^n \exp(-\lambda_i t) \langle \mathbf{e}_i, \mathbf{x}_i \rangle_B \mathbf{x}_i \rightarrow_{t \rightarrow +\infty} (\mathbf{e}_i^T B \mathbf{1}) \mathbf{1},$$

we get that $K_t \mathbf{e}_i$ converges to the constant function $K_{+\infty} \mathbf{e}_i = \sum_{j=1}^n B(i, j)$ on \mathcal{M} , as $t \rightarrow +\infty$. Finally, for any $f \in \mathcal{F}(\mathcal{M})$ the map $K_t \mathbf{f} = \sum_{i=1}^n f(\mathbf{p}_i) K_t \mathbf{e}_i$ is a linear combination of the canonical basis with the f -values as coefficients.

4.2. Feature-driven basis functions and approximation

To define a set of *shape-driven* canonical basis functions, as feature points $\{\mathbf{p}_i\}_{i \in \mathcal{A}}$ of a 3D shape we select the maxima and minima of the Laplacian eigenfunctions related to the smallest eigenvalues [RPSS10] or of the auto-diffusion maps [GBAL09]. Computing the corresponding canonical basis functions $\{K_t \mathbf{e}_i\}_{i \in \mathcal{A}}$, we get a set of maps that are intrinsically defined by the input shape and invariant to isometries. In

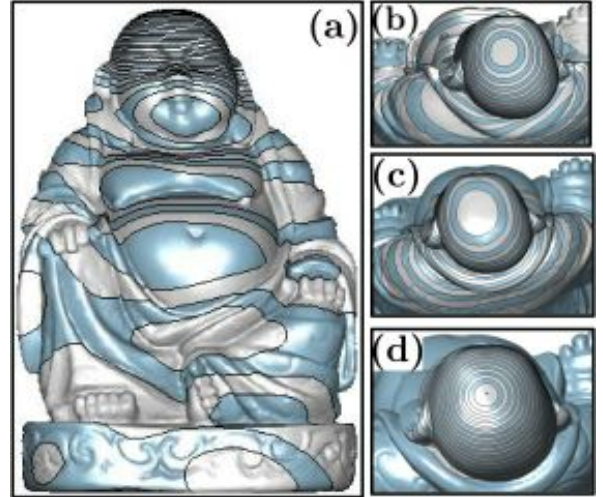


Figure 9: Comparison of the canonical basis functions computed with the (a,b) partial Laplacian eigendecomposition (8), (c) first order Taylor approximations in Eq. (9), and (d) generalized Chebyshev computation in Eq. (11).

Table 2: Timings (s:ms) related to the computation (Fig. 4) of the Laplacian matrix L , the mass matrix B , and the multi-scale function $K_t \mathbf{f}$ with the generalized Chebyshev approximation. Tests have been performed on a 1.83 GHz Intel Core Duo with 1GB 667 Mhz DDR2 SDRAM memory.

n	Comp. (L, B)	Feat. map $K_t \mathbf{f}$
1K	0.0734	0.26
5K	0.0821	0.94
20K	0.3438	11.36
40K	0.6067	13.20
80K	0.7044	16.98
100K	0.9781	54.56
200K	2.8119	67.44
400K	4.138	98.36
500K	5.5434	112.22

this way, their supports are located on prominent features of \mathcal{M} and identify semantically meaningful regions (e.g., protrusions, symmetries). Similarly to [GCO06; GMGP05; HK03; LG05; MS05; OFCD02; RPSS10], these functions provide local shape descriptors that are useful for matching, stable to noise and non-intrinsic deformations.

The shape-driven canonical basis is used to decompose a noisy scalar function $f : \mathcal{M} \rightarrow \mathbb{R}$ into the sum of a *global component*, which is defined by the f -values at the critical points with a given persistence, and a *local component*, which encodes the details of f . The difference between this approach and the least-squares projection on the Laplacian eigenvectors is the approximation of specific f -values through the use of the shape-driven canonical basis previously introduced. To this end, we select the *feature values* $\{f(\mathbf{p}_i)\}_{i \in \mathcal{A}}$, $\mathcal{A} \subseteq \{1, \dots, n\}$, associated to the critical points of f with highest persistence [Ban67; EMP06; PF09]. This choice is aimed at guar-

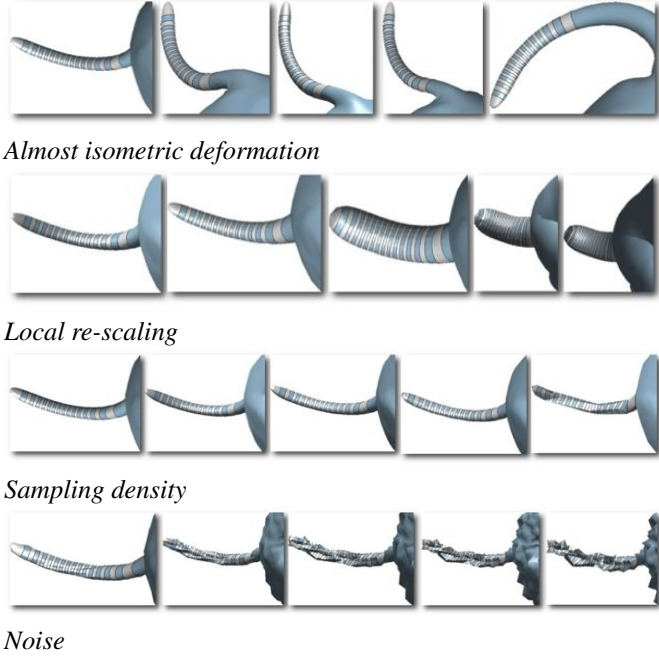


Figure 10: Robustness of the computation of the basis function induced by the wFEM heat kernel and centered at the spike of the tail. The transformation strength increases from left to right.

anteeing that a global persistent information on the behavior of the input map is preserved during the approximation. For more details on the relation between persistent critical points and the characterization of the behavior of the input map, we refer the Reader to [EMP06; PF09]. Combining the functions $\{K_t \mathbf{e}_i\}_{i \in \mathcal{A}}$ with the feature values, we define the *global component* of f constrained to \mathcal{A} as $f_{glob} := \sum_{i \in \mathcal{A}} f(\mathbf{p}_i) K_t \mathbf{e}_i$. Introducing the *local component* $f_{loc} := f - f_{glob}$ of f , we expect that f_{loc} encodes the local features, or noise, of f and f_{glob} identifies its global behavior. As shown in Fig. 12, the global component of the input scalar function is a smooth approximation of the input scalar function and the local component encodes its local details and noise. To estimate the robustness to noise, we perturb the f -values as $\tilde{\mathbf{f}} := \mathbf{f} + \mathbf{e}$, $\mathbf{e} \in \mathbb{R}^n$ and bound the difference between the corresponding embeddings as follows

$$\begin{aligned} \|K_t \mathbf{f} - K_t \tilde{\mathbf{f}}\|_B &= \|K_t \mathbf{e}\|_B \\ &= \left\| \sum_{i=1}^n \exp(-\lambda_i t) \langle \mathbf{e}, \mathbf{x}_i \rangle_B \mathbf{x}_i \right\|_B \\ &\leq \left\| \sum_{i=1}^n \langle \mathbf{e}, \mathbf{x}_i \rangle_B \mathbf{x}_i \right\|_B \\ &= \|\mathbf{e}\|_B. \end{aligned}$$

Indeed, the upper bound is proportional to the norm $\|\mathbf{e}\|_B$. For more details, we refer the Reader to [PF10].

Our experiments have shown that selecting as \mathcal{A} the set of indices of the critical points of f with a high persistence generally provides results that are smoother than using all the critical points and with an approximation accuracy of the same

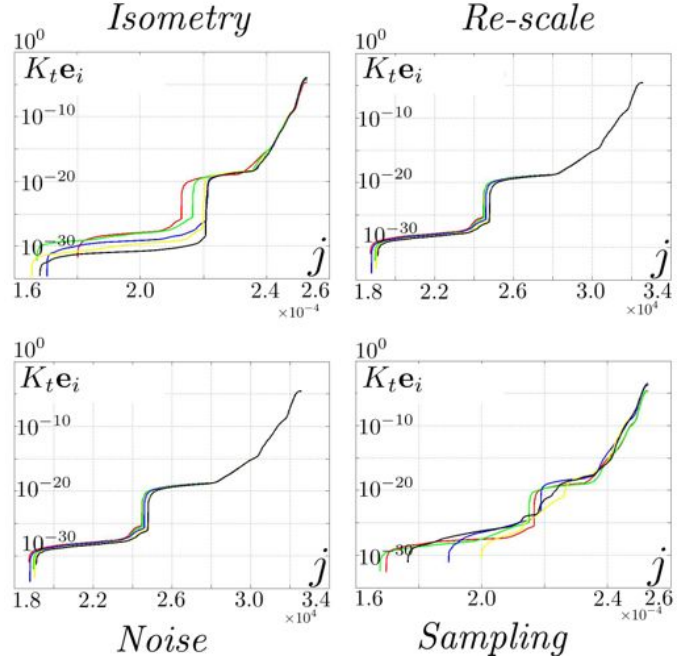


Figure 11: Behavior of the basis function $K_t \mathbf{e}_i$ centered at the extreme of the tail in Fig. 10. On the y-axis (logarithmic scale), we report the value assumed by $K_t \mathbf{e}_i$ at the point \mathbf{p}_j (x-axis). The transformation strength increases according to the following color variation: red, green, blue, yellow, and black.

order. Increasing the persistence provides a lower number of preserved critical points. In Fig. 13(a,b), the critical points of a noisy f have been simplified from 40% to 10%. Then, the set \mathcal{A} of preserved critical points defines the approximation f_{glob} ; (d) shows the level-sets of the approximations with respect to a different choice of \mathcal{A} and the final approximation is depicted in (c). For each example, the \mathcal{L}_∞ error between the input and approximated map is below 2%. In our implementation, the multi-scale hierarchy is generated by varying the parameter t on an uniform sampling of the interval $[0, \lambda_k^{-1}]$ (e.g., $k := 20$); generally, from five to ten scales $\{t_i := \frac{i}{10} \lambda_k^{-1}\}_{i=1}^{10}$ are enough to provide a satisfactory decomposition of the input map into local and global components.

5. wFEM heat kernel descriptors for shape comparison

In the following, we prove that the wFEM heat kernel is intrinsically scale-covariant (i.e., without surface normalization) and scale-invariant through a normalization of the Laplacian eigenvalues. Finally, we experimentally verify that the wFEM discretization improves the robustness of the corresponding descriptors for shape matching.

Using the heat kernel, a shape \mathcal{M} is associated to a diffusion metric that measures the rate of connectivity among the points of \mathcal{M} with paths of length t and characterizes the local/global geometric behavior of \mathcal{M} with small/large values of t . The

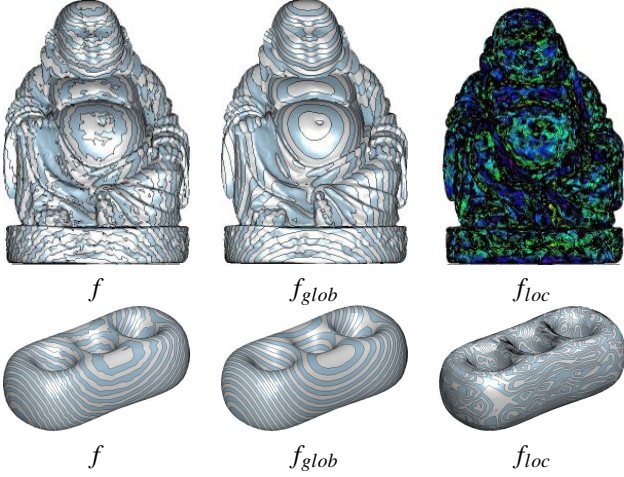


Figure 12: Level-sets of a noisy map f , its global f_{glob} and local f_{loc} component.

heat kernel also induces multi-scale [SOG09] and isometry-invariant [BBK⁺10; BK10; M09] signatures, which are used to rewrite the shape similarity problem as the comparison of two metric spaces [Rus07; MS09] equipped with diffusion distances [CL06; LKC06]. Before testing the performance of the wFEM heat kernel for shape matching, we verify that the proposed discretization is scale-invariant and scale-covariant; in this way, it satisfies two important properties for the definition of shape descriptors.

The wFEM heat kernel K_t is intrinsically *scale-covariant*; i.e., reshaping \mathcal{M} to $\alpha\mathcal{M}$ only the time component of the kernel is rescaled. In fact, the rescaling of \mathcal{M} to $\alpha\mathcal{M}$ changes the mass matrix B and the eigensystem $\{(\lambda_i, \mathbf{x}_i)\}_{i=1}^n$ of \mathcal{M} into $\alpha^2 B$ and $\{(\alpha^{-2}\lambda_i, \alpha^{-1}\mathbf{x}_i)\}_{i=1}^n$, respectively. Indeed, $K_t(\alpha\mathcal{M}) = K_{\alpha^{-2}t}(\mathcal{M})$ without an *a-posteriori* normalization. The scale-covariance of K_t is guaranteed by the mass matrix, which changes according to the surface rescaling and compensates the variation of the corresponding Laplacian spectrum. The kernel becomes *scale-invariant* (i.e., $K_t(\alpha\mathcal{M}) = K_t(\mathcal{M})$) by normalizing each eigenvalue by λ_n . In this way, the ratio λ_i/λ_n belongs to the interval $[0, 1]$ and the eigenvalue λ_n is efficiently computed using the inverse method [GV89; VL08].

To verify how the proposed discretization improves the robustness of heat kernel descriptors for shape matching, the wFEM heat kernel and diffusion distances have been evaluated using the SHREC'10 data set [BBB⁺10; BBC⁺10]. It consists of shapes modified through transformations of different strength (five degrees): the higher the number, the stronger the transformation. The transformations are: *null transformation*, *isometry* (non-rigid almost isometric deformations), *topology* (welding of shape vertices resulting in different triangulation), *micro holes* and *big holes*, *global* and *local scaling*, *additive Gaussian noise*, *shot noise*, *down-sampling* (less than 20% of the original points), *partial occlusion*, and *mixed transformation*.

In our experiments, we have normalized the Laplacian eigenvalues with respect to the eigenvalue of maximum magnitude

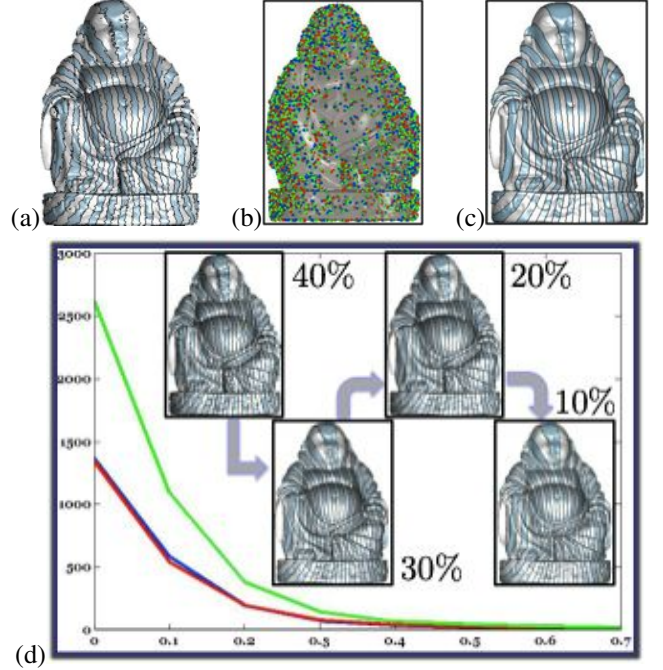


Figure 13: (a) Level-sets and (b) critical points of a noisy map f and (c) its smooth approximation $K_t f$: the maxima, minima, and saddles are shown in red, blue, and green, respectively. (d) Level-sets and number of critical points (y-axis) of the projection of f onto the basis functions associated to a different persistence (x-axis) of simplified critical points of f .

instead of the surface-area $\bar{\lambda} := \lambda / \text{area}(\mathcal{M})$. Figs. 14(b,c,d,e) show the behavior of the first 200 normalized linear FEM Laplacian eigenvalues of a set of five shapes, which have been achieved by removing small (Fig. 14(b)) and large (Fig. 14(d)) regions of a template (Fig. 14(a)). Our tests on the SHREC'10 data set have shown that normalizing the linear FEM Laplacian spectrum with respect to the eigenvalue of maximum magnitude generally provides normalized eigenvalues (Fig. 14(e,g)) that are much closer to the normalized linear FEM eigenvalues of the template. This choice is also suitable for the SHREC'10 data set because it does not contain 3D shapes when large sub-parts of the data have been removed.

For the robust feature detection and description benchmark [BBB⁺10], the number of transformations *per* shape was 45 and the total data set size was 138. Three classes of feature description methods have been compared: (i) the heat kernel signature [SOG09] with Voronoi-cot weights in Eq. (7) and feature points detected as local maxima of the signature with/without (SHK1/SHK2) simplification based on persistence homology [ZC05]; (ii) the dense signature [BBGO11] based on the Voronoi-cot (DHK1) and wFEM (DHK2) heat kernel; (iii) the spin image signatures [JH99] (SP).

For the robust large-scale shape retrieval benchmark [BBC⁺10], the total number of transformations per shape was 55 and the total number of query shapes was 715. Three classes of methods have been compared: visual simi-

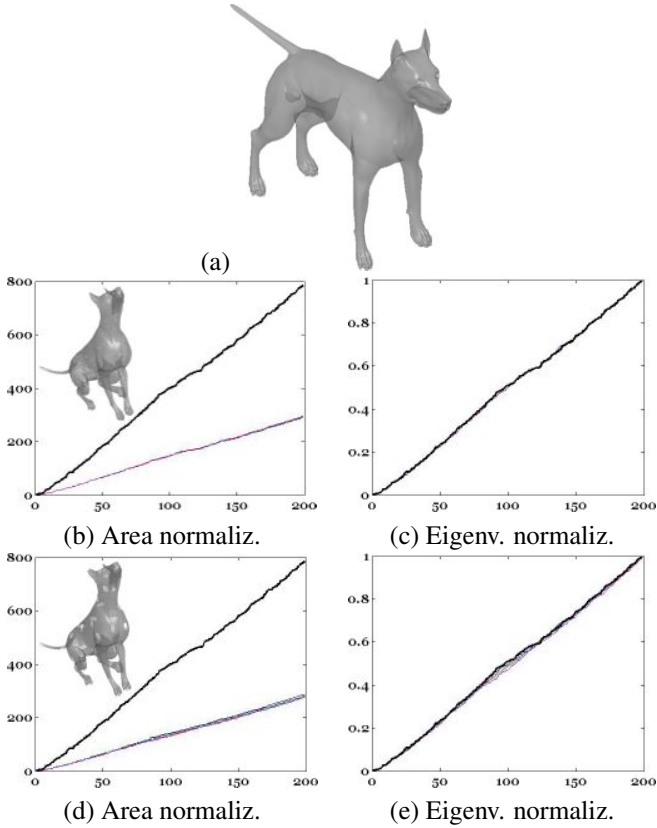


Figure 14: First 200 linear FEM Laplacian eigenvalues (colored graphs) normalized with respect to (b,d) the surface area and (c,e) the eigenvalue of maximum magnitude on a 3D shape with (b,d) holes of different sizes [BBB⁺10; BBC⁺10]. The black line represents the normalized linear FEM Laplacian of (a) the input template.

larity [LGS10; LRS10]; part-based bags of features [TCF09]; Shape-Google [BBGO11] based on the heat kernel shape descriptor using Voronoi-cot [DMSB99; PP93] or wFEM weights, with or without kernel normalization [BK10]. For the evaluation of the results, we have used the *mean average precision* (mAP); i.e., $mAP := \sum_i P(i)rel(i)$, where $rel(i)$ is the relevance of a single rank and the *precision* $P(i)$ is computed as the percentage of relevant shapes in the first i top-ranked retrieved shapes. Ideal retrieval performance results in $mAP = 100\%$.

The quality of the feature detection was measured using the *repeatability* criterion [BBB⁺10; BBC⁺10]. For each shape Y , let $\mathcal{A}(Y) := \{y_k\}_k$ be the set of detected feature points. Assuming for each transformed shape Y in the data set the ground truth dense correspondence to the null shape X to be given in the form of pairs of points $C_0(X, Y) = \{(x'_k, y_k)\}_{k=1}^{|Y|}$ (similarly for $C_0(Y, X)$), a feature point $y_k \in \mathcal{A}(Y)$ is said to be *repeatabile* if a geodesic ball $B_R(x'_k)$ of radius R around the corresponding point x'_k such that $(x'_k, y_k) \in C_0(X, Y)$ contains a feature point $x_j \in \mathcal{A}(X)$. The subset $\mathcal{A}_{R,X}(Y) \subseteq \mathcal{A}(Y)$ of repeatable fea-

Table 3: Shape comparison results. Winning feature description algorithms across transformation classes and strengths. Heat kernel signature with cotangent weights and feature points detected as local maxima of the signature without/with (SHK1/SHK2) persistence (homology) simplification. Dense signature based on Voronoi-cot (DHK1) and wFEM (DHK2) heat kernel discretization in Eqs. (7) and (6). Spin image signatures (SP).

Transf.	Strength degree				
	1	2	3	4	5
Isometry	DHK2	DHK2	DHK2	DHK2	DHK2
Topology	DHK2	DHK2	DHK2	DHK2	DHK2
Holes	DHK2	DHK2	DHK2	DHK2	DHK1
Micro holes	DHK2	DHK2	DHK2	DHK2	DHK2
Scale	SHK2	SHK2	SHK2	SHK2	SHK2
Local scale	DHK2	DHK2	DHK2	DHK2	DHK2
Sampling	DHK2	DHK2	DHK2	DHK2	DHK2
Noise	DHK1	DHK1	DHK2	SHK1	SHK2
Shot noise	DHK2	DHK2	DHK2	DHK2	DHK2
Average	DHK2	DHK2	DHK2	DHK2	DHK2

tures is given by

$$\mathcal{A}_{R,X}(Y) = \{y_k \in \mathcal{A}(Y) : \mathcal{A}(X) \cap B_R(x'_k) \neq \emptyset, (x'_k, y_k) \in C_0(X, Y)\}.$$

Then, the repeatability $rep(Y, X)$ of $\mathcal{A}(Y)$ in X is defined as the percentage $rep(Y, X) = |F_{R,X}(Y)|/|F(Y)|$ of features from $\mathcal{A}(Y)$ that are repeatable. For a transformed shape Y and the corresponding null shape X , the overall feature detection quality was measured as $(rep(Y, X) + rep(X, Y))/2$. The value of R used in the benchmark is equal to the 5% of the shapes' diameter. Features without ground truth correspondence (e.g., in regions in the null shape corresponding to holes in the transformed shape) were ignored. In the following, we briefly present the results on shape matching with wFEM heat kernels and comparison with previous work. Due to space limitation, we refer the Reader to [BBB⁺10; BBC⁺10; BBGO11] for more details on the comparison results with respect to the different shape transformations.

According to Table 3, heat kernel signatures show the best results among the compared algorithms; on average, the wFEM heat kernel provides the highest robustness among all the transformations of different strength. As reported in Table 4, among sparse descriptors (SHK1, SHK2, and SI) the best results in average repeatability are achieved by SHK1. According to the results and discussion reported in [BBB⁺10; BBC⁺10], the best results in average repeatability in local scale and sampling classes are achieved by SHK1; in micro holes and scale, the best results are provided by SHK2; in isometry, holes, noise classes, SHK1 and SHK2 have similar performances; and spin image (SI) feature descriptor performs the best in topology and shot noise classes. Among dense descriptors (DHK1 – 3), DHK1 and DHK2 show equal average performance, with FEM-based descriptor (DH2) being slightly better in the topology, local scale, sampling, and noise classes; the scale-invariant heat ker-

Table 4: Robustness of different heat kernel signature feature description algorithms, with an average number s of feature points. As metric, we use the average \mathcal{L}_2 distance between descriptors at corresponding points. Robustness of (SHK1, $s = 23$), (SHK2, $s = 9$), (SI, $s = 205$) heat kernel feature description algorithms based on features detected by the heat kernel-based feature detection algorithms [SOG09], whose feature points are detected using (i) local maxima [EMP06; CGOS09] of the heat kernel at large scales, or (ii) persistent maxima (HK2), or (iii) the salient points feature detection method described in [CCFM08; TCF09]. Robustness of (DHK1-3) dense heat kernel signature feature description algorithms using Voronoi-cot, wFEM, and cot weights for the discretization of the heat kernel.

Strength degree					
Method	1	2	3	4	5
SHK1	0.06	0.06	0.08	0.09	0.12
SHK2	0.05	0.06	0.08	0.10	0.13
SI	0.13	0.13	0.14	0.14	0.15
DHK1	0.04	0.04	0.04	0.05	0.06
DHK2	0.04	0.04	0.04	0.05	0.06
DHK3	0.10	0.10	0.11	0.12	0.13

nel signatures (DHK3) perform the best in the scale class.

As shown in Table 5, the compared methods have different performances across transformation classes. On average, similarity sensitive hashing (SS1) and Shape-Google using scale-invariant heat-kernel signatures (SG3), which represents 3D shapes as binary codes through bag-of-features embedded in the Hamming space, have the best performances on all class of transformations. In this case, we have 98, 27% mAP on the full query set. Second best in all strengths is VS2 with 94.33% mAP and at the third place we have SG3 with 90.79% mAP. Finally, VS2 and Shape-Google using heat kernel shape descriptors based on the wFEM discretization have the best robustness to sampling density; VS2 also has the best performance in mixed transformation class. Detailed shape matching results with respect to all the transformations, which have been summarized in Tables 4, 5, are reported in [BBB⁺10; BBC⁺10; BBGO11].

6. Conclusions and future work

Using the linear FEM discretization of the Laplace-Beltrami operator, we have shown that the wFEM heat kernel K_t , together with the corresponding FEM diffusion distances, is robust to the local sampling density; is efficiently approximated through the Chebyshev method; and improves the performances of matching algorithms based on heat kernel shape descriptors. In fact, the wFEM heat kernel is intrinsically scale-covariant and scale-invariant through a normalization of the Laplacian eigenvalues. The scalar product induced by K_t also makes the space $\mathcal{F}(\mathcal{M})$ of piecewise linear scalar functions on a triangulated surface \mathcal{M} a Hilbert Space, whose reproducing kernel is the linear FEM heat kernel. Finally, the wFEM heat kernel K_t

Table 5: Performances with respect to all the transformations. Visual similarity: clock matching bag of features with/without (VS1/VS2) modified manifold ranking; (VS3) geodesic sphere based multi-view descriptor. Part-based bas of features: part-based bag of words with (PB1) large number of visual words; (PB2) words with visual vocabulary computed from the training set; (PB3) visual vocabulary computed from the test set. Shape-Google using HKS local descriptor computed with (SG1) Voronoi-cot weights; (SG2) wFEM weights; (SG3) SI-HKS local descriptor computed with Voronoi-cot weights; (SS1) HKS local descriptor computed with Voronoi-cot weights and 96 bit similarity sensitive hash (mAP in %).

Strength degree					
Method	1	2	3	4	5
VS1	95.92	90.81	86.48	81.94	77.78
VS2	99.03	97.73	96.71	95.66	94.33
VS3	96.93	93.89	92.24	90.56	89.29
PB1	95.28	92.11	88.41	85.06	82.20
PB2	94.64	90.52	86.19	82.35	78.72
PB3	94.25	90.16	86.09	82.78	79.57
SG1	94.94	93.12	90.84	87.82	85.00
SG2	95.73	93.81	90.46	87.40	84.71
SG3	97.05	95.16	94.03	92.54	90.79
SS1	99.84	99.48	99.30	99.10	98.27

defines a canonical basis of $\mathcal{F}(\mathcal{M})$, which locally describes the geometry of \mathcal{M} and is useful for both shape characterization and function approximation. As main future work, we foresee the generalization of the proposed approach to point-sampled surfaces and d -dimensional data.

Acknowledgments. Special thanks are given to the anonymous Reviewers for their valuable comments, which helped us to improve the presentation and content of the paper. We are also grateful to Alexander and Micheal Bronstein for running the SHREC’10 tests on the wFEM heat kernel signatures. We acknowledge the discussion with Bianca Falcidieno, Michela Spagnuolo, and the members of the Shape Modeling Group at CNR-IMATI, Genova, Italy. This work has been partially supported by the Research Project “Methods and Techniques for the Development of Innovative Systems for Modeling and Analyzing Biomedical Data for Supporting Assisted Diagnosis”, PO CRO Programme, European Social Funding Scheme, Regione Liguria, and the FP7 Marie Curie Initial Training Networks *MultiScaleHuman* - “Multi-scale Biological Modalities for Physiological Human Articulation”.

References

- [Ban67] T. Banchoff. Critical points and curvature for embedded polyhedra. *Journal of Differential Geometry*, 1:245–256, 1967.
- [BBB⁺10] A. M. Bronstein, M. M. Bronstein, B. Bustos, U. Castellani, M. Crisani, B. Falcidieno, L. J. Guibas, V. Murino I. Kokkinos, I. Isipiran, M. Ovsjanikov, G. Patanè, M. Spagnuolo, and J. Sun. Shrec 2010: robust feature detection and description benchmark. *Eurographics Workshop on 3D Object Retrieval*, 2010.
- [BBC⁺10] A. M. Bronstein, M. M. Bronstein, U. Castellani, B. Falcidieno, A. Fusiello, A. Godil, L.J. Guibas, I. Kokkinos, Z. Lian, M. Ovsjanikov, G. Patanè, M. Spagnuolo, and R. Toldo. Shrec 2010: ro-

- bust large-scale shape retrieval benchmark. *Eurographics Workshop on 3D Object Retrieval*, 2010.
- [BBGO11] A. M. Bronstein, M. M. Bronstein, L. J. Guibas, and M. Ovsjanikov. Shape google: Geometric words and expressions for invariant shape retrieval. *ACM Transactions on Graphics*, 30, 2011.
- [BBK⁺10] A. Bronstein, M. Bronstein, R. Kimmel, M. Mahmoudi, and G. Sapiro. A Gromov-Hausdorff framework with diffusion geometry for topologically-robust non-rigid shape matching. *International Journal of Computer Vision*, 2-3:266–286, 2010.
- [BK10] M. M. Bronstein and I. Kokkinos. Scale-invariant heat kernel signatures for non-rigid shape recognition. *Proc. Computer Vision and Pattern Recognition*, 2010.
- [BN03] M. Belkin and P. Niyogi. Laplacian eigenmaps for dimensionality reduction and data representation. *Neural Computations*, 15(6):1373–1396, 2003.
- [CCFM08] U. Castellani, M. Cristani, S. Fantoni, and V. Murino. Sparse points matching by combining 3D mesh saliency with statistical descriptors. *Computer Graphics Forum*, 27(2):643–652, 2008.
- [CGOS09] F. Chazal, L. J. Guibas, S. Y. Oudot, and P.z. Skraba. Analysis of scalar fields over point cloud data. In *Proc. of Symposium on Discrete Algorithms*, pages 1021–1030, 2009.
- [CJ97] C. S. Chua and R. Jarvis. Point signatures: A new representation for 3D object recognition. *International Journal of Computer Vision*, 25(1):63–85, 1997.
- [CL06] R. R. Coifman and S. Lafon. Diffusion maps. *Applied and Computational Harmonic Analysis*, 21(1):5–30, 2006.
- [CMV69] W. J. Cody, G. Meinardus, and R. S. Varga. Chebyshev rational approximations to $\exp(-z)$ in $(0, +\infty)$ and applications to heat-conduction problems. *Journal of Approximation Theory*, 2:50–65, 1969.
- [dGGV08] F. de Goes, S. Goldenstein, and L. Velho. A hierarchical segmentation of articulated bodies. *Computer Graphics Forum*, 27(5):1349–1356, 2008.
- [DMSB99] M. Desbrun, M. Meyer, P. Schröder, and A. H. Barr. Implicit fairing of irregular meshes using diffusion and curvature flow. In *ACM Siggraph*, pages 317–324, 1999.
- [DRW10] T. K. Dey, P. Ranjan, and Y. Wang. Convergence, stability, and discrete approximation of laplace spectra. *ACM Symposium Discrete Algorithms*, pages 650–663, 2010.
- [EMP06] H. Edelsbrunner, D. Morozov, and V. Pascucci. Persistence-sensitive simplification functions on 2-manifolds. In *Proc. of the Symposium on Computational Geometry*, pages 127–134, 2006.
- [GBAL09] K. Gebal, J. A. Bærentzen, H. Aanæs, and R. Larsen. Shape analysis using the auto diffusion function. *Computer Graphics Forum*, 28(5):1405–1413, 2009.
- [GCO06] R. Gal and D. Cohen-Or. Salient geometric features for partial shape matching and similarity. *ACM Transactions on Graphics*, 25(1):130–150, 2006.
- [GMGP05] N. Gelfand, N. J. Mitra, L. J. Guibas, and H. Pottmann. Robust global registration. In *Proc. of the Symposium on Geometry Processing*, page 197, 2005.
- [GS92] E. Gallopoulos and Y. Saad. Efficient solution of parabolic equations by krylov approximation methods. *SIAM Journal of Scientific Statistical Computation*, 13:1236–1264, 1992.
- [GSCO07] R. Gal, A. Shamir, and D. Cohen-Or. Pose-oblivious shape signature. *IEEE Transactions on Visualization and Computer Graphics*, 13(2):261–271, 2007.
- [GV89] G. Golub and G.F. VanLoan. *Matrix Computations*. John Hopkins University Press, 2nd Edition, 1989.
- [HK03] A. B. Hamza and H. Krim. Geodesic object representation and recognition. In *International Conference on Discrete Geometry for Computer Imagery*, pages 378–387, 2003.
- [HSKK01] M. Hilaga, Y. Shinagawa, T. Kohmura, and T. L. Kunii. Topology matching for fully automatic similarity estimation of 3D shapes. In *ACM Siggraph*, pages 203–212, 2001.
- [JH99] A. E. Johnson and M. Hebert. Using spin images for efficient object recognition in cluttered 3D scenes. *IEEE Transactions on Pattern Analysis and Machine Intelligence*, 21(5):433–449, 1999.
- [LG05] X. Li and I. Guskov. Multi-scale features for approximate alignment of point-based surfaces. In *Proc. of the Symposium on Geometry processing*, pages 217–226, 2005.
- [LGS10] Z. Lian, A. Godil, and X. Sun. Visual similarity based 3D shape retrieval using bag-of-features. *International Conference on Shape Modeling and Applications*, pages 25–36, 2010.
- [LKC06] S. Lafon, Y. Keller, and R. R. Coifman. Data fusion and multicue data matching by diffusion maps. *IEEE Transactions on Pattern Analysis Machine Intelligence*, 28(11):1784–1797, 2006.
- [LRS10] Z. Lian, P.L. Rosin, and X. Sun. Rectilinearity of 3D meshes. *International Journal of Computer Vision*, 89(2):130–151, 2010.
- [M09] F. Mémoli. Spectral Gromov-Wasserstein distances for shape matching. In *Workshop on Non-Rigid Shape Analysis and Deformable Image Alignment*, 2009.
- [MS05] F. Mémoli and G. Sapiro. A theoretical and computational framework for isometry invariant recognition of point cloud data. *Foundations of Computational Mathematics*, 5(3):313–347, 2005.
- [MS09] M. Mahmoudi and G. Sapiro. Three-dimensional point cloud recognition via distributions of geometric distances. *Graphical Models*, 71(1):22–31, 2009.
- [MVL03] C. Moler and C. Van Loan. Nineteen dubious ways to compute the exponential of a matrix, twenty-five years later. *SIAM Review*, 45(1):3–49, 2003.
- [OFCD02] R. Osada, T. Funkhouser, B. Chazelle, and D. Dobkin. Shape distributions. *ACM Transactions on Graphics*, 21(4):807–832, 2002.
- [OMMG10] M. Ovsjanikov, Q. Mérigot, F. Mémoli, and L. Guibas. One point isometric matching with the heat kernel. *ACM Symposium on Discrete Algorithms*, pages 650–663, 2010.
- [PF09] G. Patanè and B. Falcidieno. Computing smooth approximations of scalar functions with constraints. *Computer & Graphics*, 33(3):399 – 413, 2009.
- [PF10] G. Patanè and B. Falcidieno. Multi-scale feature spaces for shape processing and analysis. In *Proc. of IEEE Shape Modeling International*, pages 113–123, 2010.
- [PP93] U. Pinkall and K. Polthier. Computing discrete minimal surfaces and their conjugates. *Experimental Mathematics*, 2(1):15–36, 1993.
- [Ros97] S. Rosenberg. *The Laplacian on a Riemannian Manifold*. Cambridge University Press, 1997.
- [RPSS10] M.R. Ruggeri, G. Patanè, M. Spagnuolo, and D. Saupe. Spectral-driven isometry-invariant matching of 3D shapes. *International Journal of Computer Vision*, 89(2-3):248–265, 2010.
- [Rus07] R. M. Rustamov. Laplace-beltrami eigenfunctions for deformation invariant shape representation. In *Proc. of the Symposium on Geometry processing*, pages 225–233, 2007.
- [RWP06] M. Reuter, F.-E. Wolter, and N. Peinecke. Laplace-Beltrami spectra as Shape-DNA of surfaces and solids. *Computer-Aided Design*, 38(4):342–366, 2006.
- [SCOIT05] O. Sorkine, D. Cohen-Or, D. Irony, and S. Toledo. Geometry-aware bases for shape approximation. *IEEE Transactions on Visualization and Computer Graphics*, 11(2):171–180, 2005.
- [SOG09] J. Sun, M. Ovsjanikov, and L. J. Guibas. A concise and provably informative multi-scale signature based on heat diffusion. *Computer Graphics Forum*, 28(5):1383–1392, 2009.
- [TCF09] R. Toldo, U. Castellani, and A. Fusiello. Visual vocabulary signature for 3D object retrieval and partial matching. *Proc. Eurographics Workshop on 3D Object Retrieval*, 2009.
- [Var90] R.S. Varga. *Scientific computation on mathematical problems and conjectures*. SIAM, 1990.
- [VBCG10] A. Vaxman, M. Ben-Chen, and C. Gotsman. A multi-resolution approach to heat kernels on discrete surfaces. *ACM Transactions on Graphics*, 29(4):1–10, 2010.
- [VL08] B. Vallet and B. Levy. Manifold harmonics. *Computer Graphics Forum* 27(2), 2008.
- [Wan09] Y. Wang. Approximating gradients for meshes and point clouds via diffusion metric. *Computer Graphics Forum*, 28:1497–1508(12), 2009.
- [XHW10] B. Xiaoa, E. R. Hancock, and R.C. Wilsonb. Geometric characterization and clustering of graphs using heat kernel embeddings. *Image and Vision Computing*, 28(6):1003 – 1021, 2010.
- [ZC05] A. Zomorodian and G. Carlsson. Computing persistent homology. *Discrete Computational Geometry*, 33(2):249–274, 2005.